Chemical interdiffusion between Na-tephritic and phonolitic melts at different T, H_2O and fO_2

Diego González-García[1,2], Florian Pohl[1], Felix Marxer[1], Stepan Krasheninnikov[1,3], Renat Almeev[1], François Holtz[1]

[1]Institut für Mineralogie, Leibniz Universität Hannover, 30167 Hannover, Germany
[2]Department of Mineralogy and Petrology, Universidad Complutense de Madrid, 28040 Madrid, Spain
[3]Institut für Geowissenschaften, Johannes Gutenberg Universität Mainz, 55128 Mainz, Germany

Correspondence to: Diego González-García (d.gonzalez-garcia@outlook.es)

Chemical interdiffusion between Na-tephritic and phonolitic melts at different T, H_2O and fO_2

Diego González-García[1,2], Florian Pohl[1], Felix Marxer[1], Stepan Krasheninnikov[1,3], Renat Almeev[1], François Holtz[1]

[1]Institut für Mineralogie, Leibniz Universität Hannover, 30167 Hannover, Germany
[2]Department of Mineralogy and Petrology, Universidad Complutense de Madrid, 28040 Madrid, Spain
[3]Institut für Geowissenschaften, Johannes Gutenberg Universität Mainz, 55128 Mainz, Germany

Correspondence to: Diego González-García (d.gonzalez-garcia@outlook.es)

Abstract. The diffusive exchange of major elements in Na-series tephrite-phonolite diffusion couples with compositions relevant to Canary Islands magmatism were determined at 300 MPa and variable H_2O concentrations (0.3 to 3.3 wt.%), temperature (1150 to 1300°C) and fO_2 (NNO-1.5 to NNO+1.7). Composition-dependent effective binary diffusion coefficients (D) were determined from concentration-distance profiles. Results show a wide range of diffusivities for different cations, consistently following the sequence Na >> Al >> K ≥ Mg = Fe = Ca > Si > Ti, with a mild diffusivity contrast (0.2-0.8 log units) between tephritic and phonolitic melts. Na is the fastest component, with diffusivities falling ~1.0 log unit above those of Si for any given conditions. An anomalously fast Al diffusion is observed, with D_{Al} falling ~0.4 log units above Si and ~0.6 log units below Na, suggesting a prevalence of Al-alkalis coupling across our range of run conditions. The relationships between log D and H_2O content in melt for all cations in an intermediate composition are strongly non-linear and can be fitted using an exponential function, with a convergence in diffusion coefficients for different temperature with increasing H_2O contents. Thus, Arrhenius analyses result in a decrease of activation energies from 222-293 at 1.7 wt% H_2O to 48-112 kJ/mol at 3.0 wt% H_2O. These results provide new data on chemical interdiffusion in Na-rich, highly alkaline melts and suggest that H_2O contents play a key role in increasing the chemical efficiency of magma mixing at low temperatures. The obtained dataset is used to test chemical controls of magma mixing in the El Abrigo ignmimbrite, Tenerife, where banded pumices involving basanitic-tephritic to phonolitic magmas are common in several compositionally bimodal ignimbrite units.

1 Introduction

The study of the major and trace element composition of the melt phase is an important tool to understand the evolution of subvolcanic reservoirs and their pre-eruptive dynamics and timescales. The chemically stratified nature of volcanic plumbing systems makes magma mixing and mingling a common process in a wide variety of magmatic environments, exerting an important influence over the petrological and geochemical evolution of melt and whole-rock compositions (Sliwinski et al., 2015; González-García et al., 2022). In crystal-poor systems, the magma hybridization process is mainly controlled by the interaction of melt phases, in which chemical exchange by major and trace cation diffusion plays a key role. Although diffusion

is a slow process occurring over small spatial scales, it takes advantage of extensive and complex contact areas between magmas resulting from advection, making it a key process controlling the chemical diversity of hybridizing magmas (Perugini et al., 2010, 2015; De Campos et al., 2011; DeVitre et al., 2019). Chemical variations along diffusion profiles can also provide valuable information on magma interaction and ascent timescales, as recently demonstrated by the application of major-element diffusivities to banded pumices and glassy tephra (González-García et al., 2023; Shamloo and Grunder, 2023), giving a complementary insight to results from diffusion modelling on zoned minerals. Moreover, cation diffusion plays an important role in several other magmatic processes such as crystal growth and dissolution, bubble growth and degassing (Zhang et al., 1989; Paisley et al., 2019; Mangler et al., 2023).

Because of this substantial field of application, the study of diffusion in melts at conditions as close as possible to those of natural volcanic systems is of major importance. Indeed, a large dataset of diffusion coefficients and Arrhenius equations has been published in the last decades (Zhang et al., 2010; Zhang and Gan, 2022) covering major elements, trace elements and volatiles in a wide variety of conditions. However, some important gaps still exist in the database. Diffusion data in Na-rich alkaline melts typical of ocean island systems are scarce, and consistent information on the effect of H_2O on cation diffusivity is difficult to find (Baker et al., 2002). The presence of dissolved H_2O is known to drastically reduce melt viscosity, and consequently increase diffusivities (Dingwell et al., 1996; Romano et al., 2003). Similarly, high Na contents and Na/K ratios such as those typical in alkaline ocean island magmas lead to an additional reduction in melt viscosity compared to K-rich melts and modify their molecular structure by decreasing the degree of polymerization (Le Losq et al., 2021). In turn, these parameters are thought to influence eruptive styles (Giordano and Dingwell, 2003; Andújar and Scaillet, 2012). To address these issues, we characterized experimentally the diffusive exchange of eight major elements between hydrous tephrite and phonolite melts from the Canary Islands, focusing on the influence of H_2O and temperature on the diffusion process. Experimental conditions were relevant to conditions prevailing during magma mixing events recognized in the Las Cañadas edifice, Tenerife (i.e. 1150-1300 ºC and 0.3-3.3 wt% H_2O and 300 MPa). The obtained experimental data provide insights into magma mixing events on the island of Tenerife. Our dataset can potentially be applied to other volcanic systems of analogous composition, such as the Laacher See (Tomlinson et al., 2020) or Mayotte (Berthod et al., 2021), among others.

2 Materials and Methods

2.1 Starting materials

Two natural eruption products which are representative of the Canary Islands volcanism were selected as experimental starting materials (Table 1). The mafic endmember (PF21) is a tephrite sampled in the Duraznero crater, which was built during the 1949 San Juan eruption on the island of La Palma (Klügel et al., 2000; Fuchs, 2014). Such tephritic composition is common in the historical volcanism in the Cumbre Vieja edifice (Klügel et al., 2000, 2005; Pankhurst et al., 2022) and it also resembles tephritic lava flows in the Diego Hernández Formation (DHF) of the Las Cañadas volcanic edifice, Tenerife (Bryan et al., 2002) in both major and trace element contents. These tephrites represent a widespread step in the differentiation of primitive

basanitic magmas in the Canary archipelago and are considered as a common endmember for magma mixing events in the DHF (Wolff, 1985; Bryan et al., 2002; Sliwinski et al., 2015; González-García et al., 2022).

Table 1. Composition of starting endmembers (both original starting glass and those from Fe-poor experiments DC-03 and DC-04), and the TP55 intermediate composition to which most diffusivities are referred to throughout this work (see text for details). *n* is the number of averaged EPMA analyses. H_2O concentrations in DC-03 and DC-04 were determined by FTIR.

Type	Tephrite	Phonolite	Tephrite	Phonolite	Tephrite	Phonolite	Tephri-ph.
Sample	PF21	ABP-F	DC-03	DC-03	DC-04	DC-04	TP55
n	12	12	6	6	5	6	12
wt%							
SiO_2	47.34	61.78	48.72	62.68	49.27	62.15	55.02
TiO_2	3.38	0.77	3.49	0.77	3.46	0.78	1.80
Al_2O_3	15.77	18.41	15.71	17.74	15.77	18.51	17.59
FeO_t	10.58	3.25	5.47	0.58	5.48	0.62	6.40
MnO	0.20	0.21	0.20	0.11	0.19	0.13	0.19
MgO	4.94	0.60	5.11	0.62	5.08	0.62	2.79
CaO	9.19	1.64	9.43	1.75	9.28	1.78	5.25
Na_2O	5.21	8.37	5.91	7.80	5.68	7.75	6.88
K_2O	2.30	5.54	2.41	5.46	2.41	5.51	3.79
P_2O_5	0.74	0.08	0.68	0.09	0.72	0.08	0.29
H_2O*	-	-	1.24	1.24	1.10	1.10	-
Total	99.65	100.65	98.36	98.85	98.43	99.03	100.00

The evolved endmember (ABP-F) is a phonolite originating from aphyric white pumices of the El Abrigo ignimbrite (González-García et al., 2022). Phonolites of similar composition are widespread in all ignimbritic units of the DHF (Bryan et al., 2002; Martí et al., 2020) as well as the Teide-Pico Viejo system (Ablay et al., 1998; Dorado et al., 2021) and are the result of protracted magma differentiation and storage in shallow (< 5 km) reservoirs of the Las Cañadas volcano, and in the currently active Teide-Pico Viejo system (Andújar et al., 2008, 2010). Phonolites are also present in La Palma and are occasionally involved in magma mixing events and represented in historical volcanism on the island (Johansen et al., 2005; Klügel et al., 2022).

These starting materials were crushed and powdered in a ring mill, and subsequently melted at 1600°C for 4 h in a Nabertherm box furnace at ambient pressure. After quenching in water, the resulting glasses were ground in an agate ball mill and melted again at the same conditions to ensure chemical homogeneity. After three melting and crushing cycles, the resulting glass was crushed again to obtain the final starting material powders for experimental capsules.

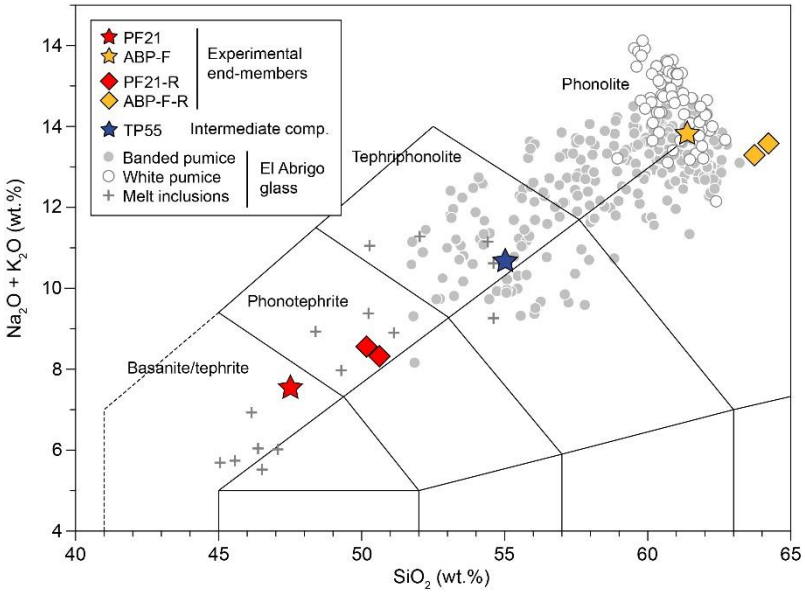

Figure 1. Total alkalis-silica diagram showing the compositions of initial tephritic (PF21) and phonolitic (ABP-F) endmembers, as well as Fe-poor endmembers from experiments DC-02 and DC-03 (PF21-R and ABP-F-R). The intermediate composition (TP55) for which diffusivities are derived is also shown. Glass compositions from El Abrigo pumices (González-Garcia et al., 2022) are plotted for comparison.

2.2 Experimental setup

Hydrous starting glasses were produced at high pressure and temperature using $Au_{80}Pd_{20}$ alloy capsules with an inner diameter of 5.0 mm and a length of 35 mm. The capsules were filled with glass powder and, when necessary, appropriate amounts of distilled water, in several steps. Glasses of both end-member compositions were produced as nominally dry (ND, i.e. no added water) and nominal H_2O concentrations of 1.5, and 3 wt.%. After loading, capsules were welded shut, and glasses were synthetized at 300 MPa and 1200 °C in two different Internally Heated Pressure Vessels (IHPV; Berndt et al., 2002). A first set of starting glasses (experiment set A) was synthesized at fO_2 conditions close to the Ni-NiO buffer (NNO, equivalent to QFM+0.6) at H_2O-saturated conditions in an IHPV equipped with an H_2 Shaw membrane for fO_2 monitoring (Berndt et al., 2002) using an Ar-H_2 pressure medium, with synthesis duration of 72 h. A second set of glasses (experiment set B) was synthesized at the intrinsic fO_2 of the IHPV (Ar-only pressure medium), with fO_2 close to NNO+2.3 at H_2O-saturated conditions, as verified using CoPd redox sensors (Taylor et al., 1992; Marxer and Ulmer, 2019). Temperatures were controlled with S-type (Pt-$Pt_{90}Rh_{10}$) thermocouples and pressure was monitored with calibrated Burster pressure transducers. For all runs, the capsules were quenched isobarically after switching off the power supply of furnace, resulting in an initial cooling rate of ca. 200 °C/min. After the synthesis, the glasses recovered from the capsules were cut to obtain cylinders with a length of ca. 3-4 mm, and each cylinder was finely polished on one side.

Diffusion experiments were run using the diffusion couple method (Baker, 1989, 1990; Nowak and Behrens, 1997), in which the polished side of phonolitic and tephritic glasses with the same nominal water content are juxtaposed to each other and placed inside an Au_{80}-Pd_{20} capsule with an inner diameter of 5.1 mm. The denser tephritic glass was placed in the bottom position to avoid gravitational instability during the experiment. The capsules were closed by arc-welding and pre-compressed in a cold seal pressure vessel (CSPV) to check for tightness.

The diffusion experiments were run in the same IHPVs that were used for glass synthesis, at temperatures ranging from 1150 to 1300 °C and a constant pressure of 300 MPa. Table 2 shows a summary of run conditions for all experimental charges. The vessels were pressurized with Ar-H_2 (set A) or Ar (set B) and the experiments were run for 2 h and 4 h (plus one additional zero-time experiment). The heating ramps from ambient temperature to final dwell temperature were 30 °C/min in set A experiments, and 50 °C/min in set B experiments. After each run, a rapid quench device (Berndt et al., 2002) was activated, allowing the capsule to fall into the cold part of the vessel and cool quickly, with quenching rates up to 50 ºC/s. A total of 13 experiments were run successfully and utilized for the present study (Table 2).

2.3 Analytical procedures

From the starting glasses, 10-20 mg glass chips from both ends of the capsule were used to measure H_2O contents by pyrolysis and subsequent Karl Fischer titration (KFT; Behrens, 1995; Behrens et al., 1996). Iron oxidation state ($Fe^{3+}/\Sigma Fe$ ratio) was measured by a colorimetric wet-chemical analysis (Schuessler et al., 2008). Small glass chips (5-20 mg) from the two ends of the post-synthesis glass cylinders were powdered, dissolved in HF and analysed by absorption spectrometry in the visual spectrum using a Shimadzu UV 1800 UV/VIS spectrometer. This method allows determining the $Fe^{2+}/\Sigma Fe$ ratios with high precision (typically within <3%).

After the diffusion couple experiments, each capsule was cut longitudinally in two halves. From one of them, a double polished section was prepared, with thickness between 100 and 300 µm. The second half was mounted in 1-inch epoxy resin mounts and polished. H_2O concentrations were measured by FTIR in the double polished sections, and an electron probe micro-analyzer (EPMA) was employed for determination of major element concentrations in the epoxy-mounted experimental charges.

In the resulting diffusion couples, H_2O concentrations were obtained by FTIR using a Bruker IFS88 spectrometer coupled to an IR-Scope II microscope at the Institute of Mineralogy, Leibniz Universität Hannover. Absorption coefficients determined for a Na-rich phonolite glass from Teide volcano (Carroll and Blank, 1997), were applied to quantify H_2O concentrations, namely $\varepsilon_{4500} = 1.25 \pm 0.3$ L mol^{-1} cm^{-1} and $\varepsilon_{5200} = 1.10 \pm 0.10$ L mol^{-1} cm^{-1}. No absorption coefficients are published for tephritic glass, but we used values published for compositionally close shoshonitic glass by Vetere et al. (2011), i.e. $\varepsilon_{4500} = 0.80 \pm 0.06$ L mol-1 cm-1 and $\varepsilon_{5200} = 1.03 \pm 0.03$ L mol^{-1} cm^{-1}. To estimate melt density, we used the equations provided by Carroll and Blank (1997) and Vetere et al. (2011). Using these data, water concentrations were estimated by using the modified Beer-Lambert law (Stolper, 1982).

Major element oxide concentration profiles (SiO_2, TiO_2, Al_2O_3, FeO_t, MgO, MnO, CaO, Na_2O, K_2O and P_2O_5) were obtained with a JEOL JXA-iHP200F Hyper Probe electron microprobe, equipped with 5 WDS spectrometers, at the Institute of Mineralogy, Leibniz Universität Hannover. Operating conditions were an accelerating voltage of 15 kV, a beam current of 4 nA and a defocused beam diameter of 12 µm to minimize alkali loss. Accuracy is less than 3 % for concentrations > 1 wt.% except for Ca and K, which have an accuracy of < 5 %. For most experiments, two parallel transects were obtained with different lengths and resolution, to allow capturing the widely varying diffusion rates of all major elements (especially Na). In Transect 1, intervals between analytical spots were kept as small as possible (typically 15-20 µm). In contrast, the second profile spanned 3 to 4 mm across the interface with separation between analytical spots in the range of 30-40 µm. This second profile also allowed to check for possible disturbances caused by convection in the experiments. Precision and accuracy were determined by measuring VG-568 (rhyolite) and VG-2 (basalt) reference glasses (Jarosewich et al., 1980; Helz et al., 2014).

2.4 Correction for experimental times

Nominal experimental dwells of 2 and 4 hours were defined, and actual dwell times were registered for each experiment. However, due to the activation of the diffusion process at a certain temperature before reaching target experimental temperature, experimental dwell times need to be corrected by incorporating the effect of heating-up ramps. Thus, effective experiment durations were calculated by assuming an Arrhenian behaviour of diffusivity during heat-up ramps and integrating the diffusivity as a function of T with respect to t during that interval (Zhang and Behrens, 2000). Thus, the effective heating time (t_{eff}) can be calculated with the following expression (Koepke and Behrens, 2001):

$$t_{eff} = \int \frac{D_{T(t)}}{D_{Texp}} dt = \int exp\left(\frac{E_a}{R} \cdot \left(\frac{1}{T(t)} - \frac{1}{T_{exp}}\right)\right) dt \quad (1)$$

where $D_{T(t)}$ is diffusivity as a function of temperature, which is itself a function of time, $T(t)$; D_{Texp} is the diffusivity at the experimental dwell temperature (T_{exp}); E_a is the activation energy and R is the ideal gas constant. As a first approach, an E_a value of 150 kJ/mol was used, which is similar to the finally obtained values from Arrhenius analysis (see section 4.4); resulting in calculated effective heating times in the order of 180 s to 500 s. Final effective experiment durations are listed in Table 2. The high cooling rates resulting from rapid quench allow to assume an instantaneous cooling with no effect on effective run duration.

2.5 Determination of composition-dependent diffusion coefficients

Diffusion in natural, multicomponent systems is a complex phenomenon. In such cases, the diffusion of a component not only depends on its own gradient, but it is also dependent on the gradients of the other components of the system (Chakraborty et al., 1995b, a; Liang, 2010). This dependence can be rigorously described using a multicomponent diffusion matrix, requiring specific experimental strategies. Although multicomponent diffusion matrixes have been obtained for up to 7- and 8-component systems (Guo and Zhang, 2016, 2018), such an approach has never been carried out for systems with large compositional gradients, and thus it is out of the scope of this work. Instead, here we use the effective binary diffusion (EBD)

approach, a simplified procedure in which the diffusivities of each component are treated as binary diffusivities, with all the other components considered as a single component. Diffusivities obtained via this approach are therefore apparent diffusivities that are not necessarily comparable to those obtained in compositionally different systems.

Due to the variable bulk glass composition along the analysed profiles, a concentration-dependent procedure for the determination of elemental diffusivities must be used. EBD coefficients were obtained from measured concentration-distance profiles by the modified Boltzmann-Matano methodology of Sauer and Freise (1962) (hereafter SF), which does not require the knowledge of the Matano interface. In particular, the analytical solution for one-dimension, molar volume independent diffusion from Sauer and Freise (1962) was used:

$$D(x) = \frac{1}{-2t(\partial c/\partial x)}\left[(1-c(x))\int_x^{\infty} c\,dx + c(x)\int_{-\infty}^{x}(1-c(x))dx\right] \quad (2)$$

where $c(x)$ is the normalized concentration of the diffusing component, with $c(x) = 1$ at $x = -\infty$ and $c(x) = 0$ at $x = +\infty$. A modification of the Python programming language script (Oliphant, 2007) used by González-Garcia et al. (2018) was used to calculate composition-dependent diffusivities from the SF procedure.

The SF method requires that the variation of molar volume of the melt along the diffusion profile is non-significant. To check this point, we used the Bouhifd et al. (2015) formulation to obtain the molar volume of tephritic and phonolitic melts at our experimental conditions, resulting in a variation of less than 8%. This value is within the error of the SF method itself and will have no impact on obtained diffusivities. Another limitation of the SF method is that *D* cannot be accurately obtained at the endmember compositions, and for this reason we restrict the calculation of diffusivities in our profiles from 20 to 80% of the endmember compositional range.

3 Results

3.1 Starting glasses and diffusion couples

All synthesis experiments resulted in homogeneous bubble-free glasses. Phonolitic glasses were crystal-free, however tephritic glasses showed variable amounts of quench crystals produced during experiment cool-down. In contrast. diffusion couple runs resulted in crystal- and bubble-free glasses, as observed in SEM BSE imaging. This was corroborated by a zero-time experiment performed at 1200 °C and 0.3 wt.% H_2O, which showed that all quench crystals formed during the synthesis phase of the tephritic glasses had effectively dissolved upon heating and before reaching the experimental temperature (Supplementary Figure 1).

H_2O contents measured by KFT and FTIR in starting materials and diffusion couples agree well with intended concentrations, except for the nominally dry glasses of experiment set A. In these experiments, water contents measured in starting glasses were 0.8-1.1 wt.%, resulting from reduction of Fe_2O_3 in the starting material and H_2 influx through the capsule walls. In experiment set B, the same effect resulted in H_2O contents of 0.3-0.5 wt%. In the diffusion couples, H_2O concentrations measured by FTIR along a line centred in the interface of the experiments proved to be constant or close to constant for each

experiment. Variations along the line were not higher than 10 %, and hence the average of analyzed spots was assumed as H_2O concentration value for each experiment (Table 2).

Measured molar $Fe^{3+}/\Sigma Fe$ ratios in starting glasses are provided in the Supplementary Materials. Both set A tephritic and phonolitic glasses show similar trend, with $Fe^{3+}/\Sigma Fe$ varying from 0.1 to 0.2 with increasing H_2O contents (see Supplementary Figure 2). However, for Set B glasses, the observed trends differ for phonolite and tephrite, with $Fe^{3+}/\Sigma Fe$ varying from 0.25 to 0.5 for the tephrite, and from 0.45 to 0.65 for the phonolite, and again with an increasing trend with increasing H_2O owing to the more oxidizing conditions in H_2O-rich melts. This is a result of the fO_2 buffering mechanism in the IHPV. Synthesis runs with low H_2O content performed at reducing conditions suffered from loss of iron to the Au-Pd alloy capsule, resulting in a relative loss of ca. 50 and 70% of FeO in phonolitic and tephritic glasses, respectively (Table 1). This effect is only significant in the two ND experiments.

In Set A synthesis experiments, the H_2 partial pressure in the IHPV was adjusted accordingly to buffer fO_2 close to the NNO equilibrium and indeed the obtained intrinsic oxygen fugacity values were between NNO-0.1 and NNO+0.8 (base on the amount of H_2 intruduced in the vessel). However, these values only correspond to experimental fO_2 if the charges are H_2O-saturated. In H_2O-undersaturated runs, final fO_2 is shifted towards more reducing values by the term $2 \cdot log(aH_2O)$, where aH_2O is the H_2O activity in the charge. In order to apply this correction, aH_2O was approximated by $XH_2O = H_2O_{measured}$ (mol %) / $H_2O_{saturation}$ (mol %). H_2O saturation values were obtained using the MagmaSat solubility model (Ghiorso and Gualda, 2015). Consequently, experimental oxygen fugacity in the synthesis runs varied between NNO-1.7 and NNO-0.3 (Supplementary Table 1). Similarly, in Set B synthesis experiments (run at NNO+2.3 for $aH2O = 1$), final experimental fO_2 ranged between NNO-0.1 and NNO+1.7. In both cases, more oxidizing conditions correspond to H_2O-rich experiments.

3.2 Diffusion data

Concentration-distance profiles of 9 of the 10 major oxides measured in the diffusion couple runs resulted in monotonic diffusion profiles, with no evidence of uphill diffusion. Figure 2 shows an example of concentration-distance profiles measured with the EPMA, and the complete dataset is included in the Supplementary Materials. As expected from compositional contrast, all profiles are asymmetric and extend deeper into the tephritic half of the diffusion couple except for Na, which shows the opposite behavior. This dataset allows an effective binary diffusion (EBD) approach (Zhang et al., 2010). In contrast to other oxides, the MnO profile shows strong signs of uphill diffusion (Figure 2b), resulting from multicomponent diffusion effects, and thus was left out of the EBD analysis.

The application of the SF equation to the diffusion profiles led to continuous variations of D with distance across the profile (Figure 3), and hence, with bulk glass composition. As already noted by observing the shape of concentration-distance profile, most components show an inverse correlation between SiO_2 content and D, with the only exception of Na, which shows the opposite behavior. Due to the intrinsically fast diffusivity of Na, its diffusion coefficient could only be determined in the low-T and/or low-H_2O experiments. In the remaining experiments, Na diffusion reached the ends of the experimental charges, and therefore the experiment lost its characteristic of semi-infinite medium, leading to strongly underestimated Na diffusivity. In

the experiments where *D* was determined for Na, it showed the fastest diffusion among major elements, being consistently ~1 order of magnitude faster than Si. Surprisingly, Al has the second fastest diffusivity, falling approx. 0.5-0.6 log units below Na and ~0.4 log units above Si for all experiments. This is an unexpected result, since the network-forming character of Al^{3+} cations should result in diffusivities close to that of Si and Ti, as observed in most literature data (see section 4.5). The group of Mg-Fe-Ca-K display similar diffusivities but falls always between Al and Si. Finally, Ti is the slowest diffusing component, showing similar or lower values compared to Si. In comparison to the diffusion couple experiments carried out by González-Garcia et al. (2017) using shoshonite-rhyolite couples, results from tephrite-phonolite couples are highlighted by (1) a lesser prevalence of diffusive coupling to Si, resulting in a wider dispersion of diffusivities; and (2) a lack of uphill diffusion phenomena, with the only exception of Mn.

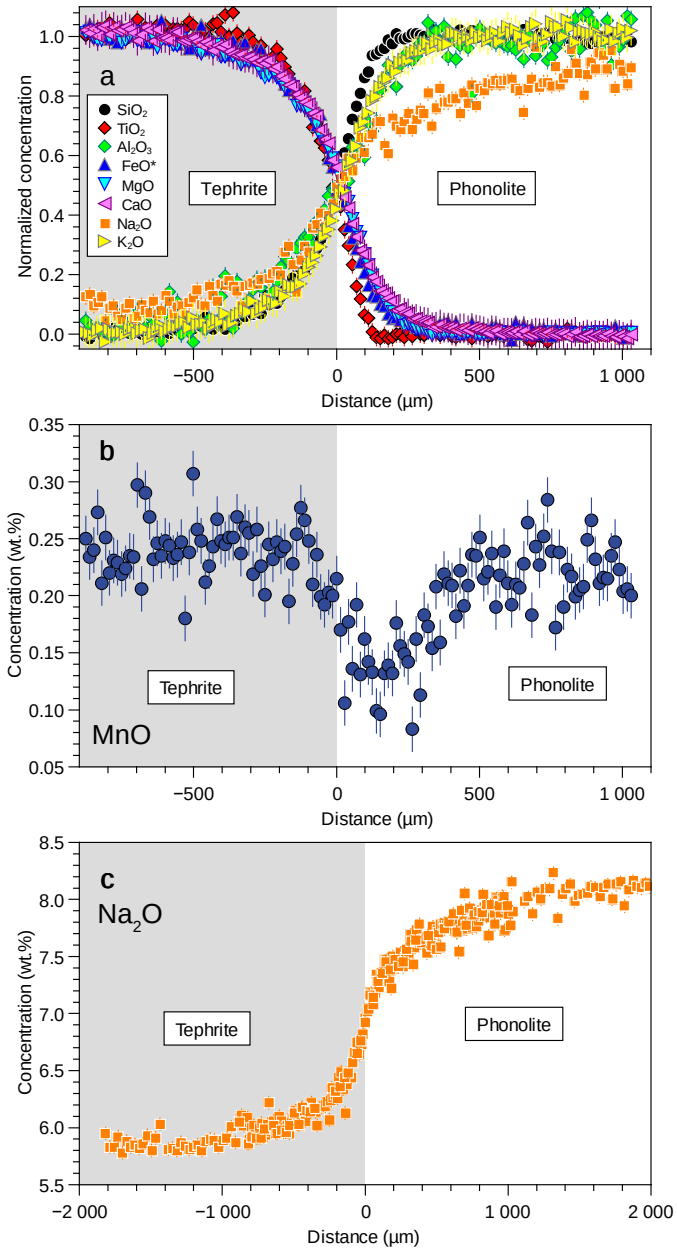

Figure 2. (a) Major element oxide concentration-distance profiles measured in experiment DCB-09, with concentrations normalized for endmember concentrations (C_{min} = 0 and C_{max} = 1). (b) MnO profile showing prominent uphill diffusion. (c) full Na_2O profile showing the greater extension of the diffusive zone (note the different length scale). Where not shown, error bars are smaller than the symbol.

4 Discussion

4.1 Compositional dependence

One of the main factors influencing cation diffusion in silicate melts is the melt chemical composition. Diffusion of divalent, trivalent and tetravalent cations is usually faster in silica poor, depolymerized melts than in silica-rich, polymerized melts, while the reverse is usually true for monovalent cations (e.g. (Zhang et al., 2010). As already visible in the asymmetry of composition-distance profiles, there is a clear compositional dependence in our tephrite-phonolite couples, and the SF analysis clearly shows this effect (Figure 4a).

To quantify the degree of compositional dependence of major cation diffusion, we can use the ratio of the diffusion coefficients for 51 wt.% SiO_2 and the 59 wt.% SiO_2 (D_{51}/D_{59}). For the 1250 ºC experiment series, we find that compositional dependence is higher in the nominally dry experiments, where D_{51}/D_{59} values are between 1.5 to 5 (equal to 0.2 to 0.7 log unit difference between the tephritic and phonolitic compositions; Figure 4b). For H_2O contents larger than 1 wt%, the ratio D_{59}/D_{51} levels down to 1.1-1.5 (< 0.2 log unit difference). Again, the exception is Na, which follows the expected behaviour for monovalent cations and diffuses up to 0.2 log units faster in phonolite than in tephrite.

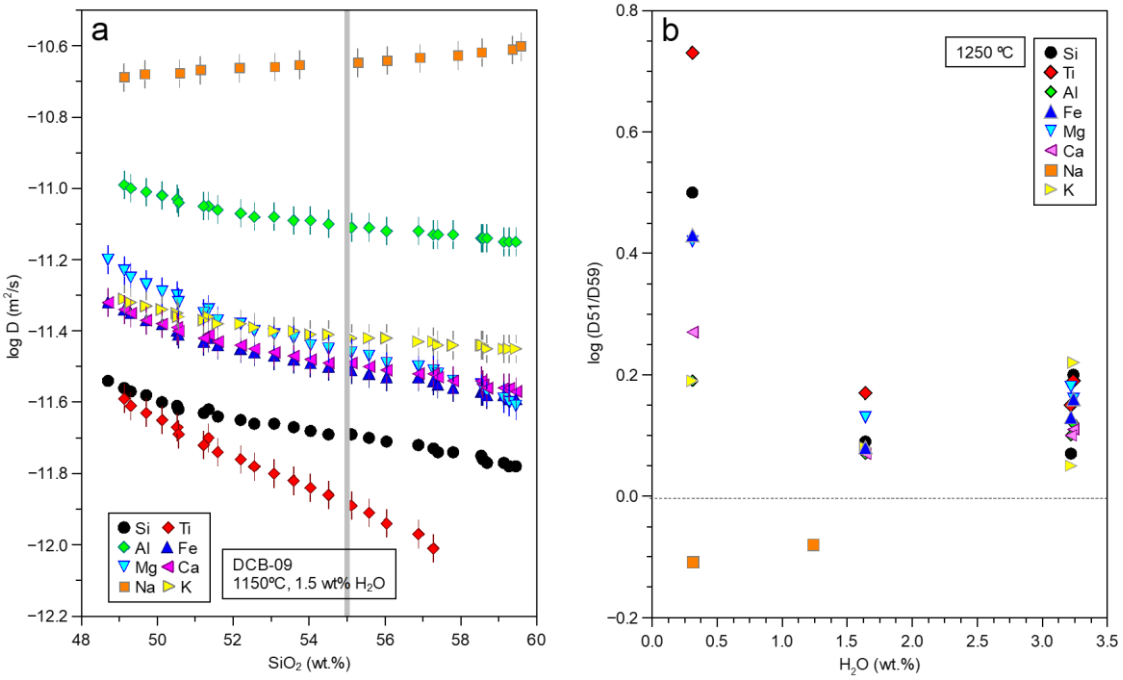

Figure 3: Concentration dependence of major element diffusivities in tephrite-basanite couples. (a) Diffusion coefficient vs SiO_2 concentration along run DCB-09, resulting from SF analysis. The vertical thick line indicates the TP55 composition used as proxy for diffusion coefficients throughout the text. (b) Variation of the compositional dependence of diffusion coefficients with H_2O content at 1250 ºC, using the ratio D_{51}/D_{59} (ratio between diffusivities at 51 ad 59 wt.% SiO_2) as index.

Due to the rather mild compositional dependence for most elements, we have chosen an intermediate composition equivalent to 55 wt.% SiO_2 (tephriphonolite) as index, for which the diffusive behaviour of major components will be described from now on. This melt composition will be hereafter referred to as TP55 (Table 1), and the full dataset of diffusion coefficients is given in Table 2.

Table 2: Experiment parameters and diffusivities obtained for the TP55 composition.

Experiment Set A					
Experiment	DC-03	DC-04	DC-05	DC-06	DC-07
Eff. Time (s)	14636	14726	7445	7680	7200
T (ºC)	1250	1200	1150	1200	1250
H_2O (wt.%)[a]	1.24 ± 0.10	1.10 ± 0.05	2.99 ± 0.21	2.98 ± 0.35	3.24 ± 0.19
XH_2O[b]	0.20	0.18	0.46	0.46	0.50
log fO_2	NNO-1.41	NNO-1.51	NNO-0.67	NNO-0.68	NNO-0.61
log D (m^2/s)					
Si	-11.34 ± 0.04	-11.97 ± 0.04	-11.01 ± 0.04	-10.93 ± 0.04	-10.85 ± 0.04
Ti	-11.53 ± 0.04	-12.02 ± 0.04	-11.29 ± 0.04	-11.28 ± 0.04	-11.17 ± 0.04
Al	-10.92 ± 0.03	-11.55 ± 0.04	-10.41 ± 0.04	-10.26 ± 0.04	-10.35 ± 0.03
Fe_t	-11.15 ± 0.04	-11.72 ± 0.04	-10.84 ± 0.04	-10.73 ± 0.04	-10.75 ± 0.04
Mg	-11.25 ± 0.04	-11.77 ± 0.04	-10.84 ± 0.04	-10.82 ± 0.04	-10.73 ± 0.04
Ca	-11.26 ± 0.04	-11.82 ± 0.04	-10.84 ± 0.04	-10.78 ± 0.04	-10.74 ± 0.04
Na	-10.51 ± 0.03	-11.02 ± 0.04	-10.23 ± 0.04	-	-
K	-11.19 ± 0.04	-11.70 ± 0.04	-10.72 ± 0.04	-10.78 ± 0.04	-10.66 ± 0.04

Experiment Set B							
Experiment	DCB-02	DCB-04	DCB-07	DCB-09	DCB-10	DCB-11	DCB-12
Eff. Time (s)	14899	14933	14605	14720	7434	7290	14684
T (ºC)	1250	1300	1250	1150	1250	1200	1200
H_2O (wt.%)[a]	0.31 ± 0.04	0.31 ± 0.03	1.64 ± 0.09	1.66 ± 0.06	3.22 ± 0.10	2.93 ± 0.06	1.69 ± 0.05
XH_2O[b]	0.05	0.05	0.26	0.26	0.49	0.45	0.27
log fO_2	NNO-0.28	NNO-0.28	NNO+1.13	NNO+1.14	NNO+1.68	NNO+1.61	NNO+1.16
log D (m^2/s)							
Si	-12.20 ± 0.05	-11.29 ± 0.04	-11.03 ± 0.04	-11.69 ± 0.04	-10.82 ± 0.04	-10.96 ± 0.04	-11.37 ± 0.04
Ti	-12.31 ± 0.05	-11.43 ± 0.04	-11.18 ± 0.04	-11.88 ± 0.04	-11.04 ± 0.04	-11.15 ± 0.04	-11.60 ± 0.04
Al	-11.68 ± 0.04	-10.67 ± 0.03	-10.54 ± 0.03	-11.10 ± 0.04	-10.33 ± 0.04	-10.51 ± 0.04	-10.95 ± 0.04
Fe_t	-12.06 ± 0.04	-11.21 ± 0.04	-10.97 ± 0.04	-11.50 ± 0.04	-10.73 ± 0.04	-10.87 ± 0.04	-11.30 ± 0.04
Mg	-12.00 ± 0.04	-11.09 ± 0.04	-10.91 ± 0.04	-11.45 ± 0.04	-10.64 ± 0.04	-10.80 ± 0.04	-11.24 ± 0.04
Ca	-12.00 ± 0.04	-11.07 ± 0.04	-10.82 ± 0.03	-11.49 ± 0.04	-10.60 ± 0.04	-10.80 ± 0.04	-11.23 ± 0.04
Na	-11.09 ± 0.04	-	-	-10.65 ± 0.04	-	-10.01 ± 0.04	-10.53 ± 0.04

K	-11.94 ± 0.04	-11.06 ± 0.04	-10.84 ± 0.04	-11.41 ± 0.04	-10.54 ± 0.04	-10.73 ± 0.04	-11.19 ± 0.04

All diffusivities correspond to a composition of 55 wt.% SiO_2 (19.7 mol% Si), referred to as TP55 in the text. D in m^2/s.
[a] H_2O contents are the average of several FTIR measurements in each experiment.
[b] XH_2O calculated as H_2O(experiment)/H_2O(saturation) in mol%. H_2O saturation was calculated using the MagmaSat Model (Ghiorso and Gualda, 2015).

4.2 Fe diffusion

The varying fO_2 experimental conditions resulted in variable Fe oxidation state (Fe3+/ΣFe ratio) in experiment sets A and B, as already observed in Supplementary Figure 2. Due to the different structural role of Fe^{3+} (network-former) and Fe^{2+} (network-modifier), the diffusivities of both species are expected to be different, with Fe^{3+} showing lower diffusivities resulting from higher bond strength (Zhang et al., 2010). Therefore, the measured D of total Fe is expected to be intermediate between that of Fe^{2+} and Fe^{3+}. Our measured diffusion dataset can be used to put some fist-order constrains to the differential diffusivity of Fe^{2+} and Fe^{3+} in the tephrite-phonolite system. Since Fe^{3+}/ΣFe was not determined in the diffusion couples, we used its relationship with estimated fO_2 in the synthesis runs (Supplementary Figure 3) to obtain a tentative estimate of Fe^{3+}/ΣFe in the diffusion couples (Figure 4). To avoid the effects of different experimental conditions, Fe diffusivities from each run were normalized to that of Mg from the same experiment. The results show that the effect of oxygen fugacity in Fe diffusion is resolved in our experimental dataset (Figure 4a). D_{Fe}/D_{Mg} values for Set B are below 0.9, whilst in the more reducing experiments D_{Fe}/D_{Mg} increases to 0.9-1.3. From this data and the linear fit in figure 4b, the difference in diffusivity of Fe^{3+} and Fe^{2+} can be estimated. Although associated errors are large, our results suggest that Fe^{2+} diffusivity in the tephrite-phonolite system is in the order of 3 to 5 times faster than that of Fe^{3+} for a given T and H_2O content (Figure 5b).

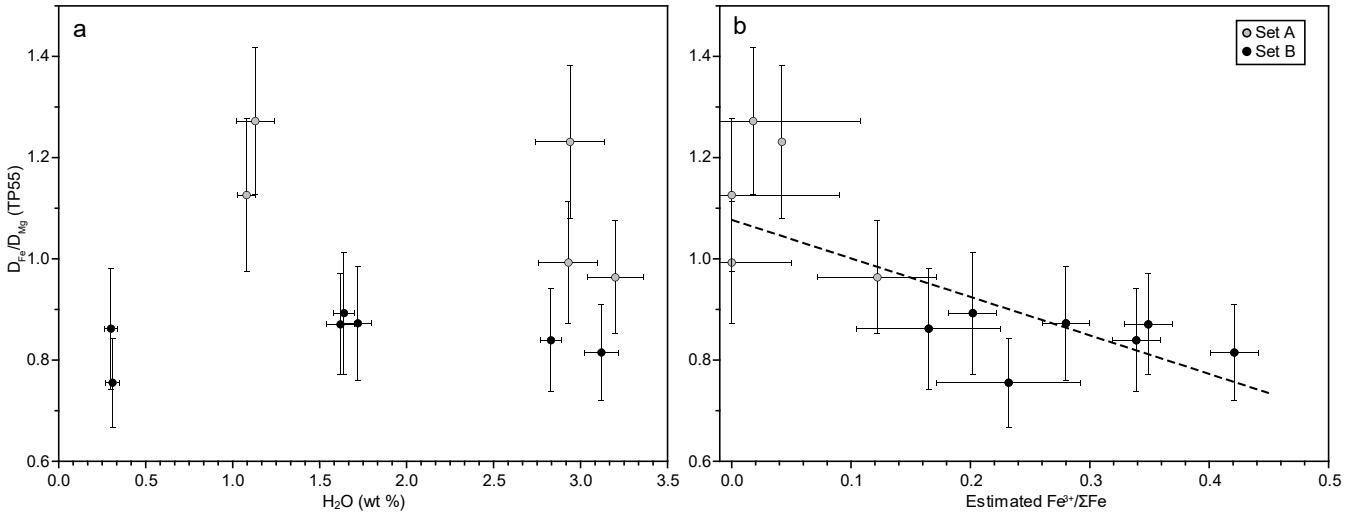

Figure 4: Mg-normalized Fe diffusivities (D_{Fe}/D_{Mg}) as a function of (a) experimental H_2O content and (b) estimated $Fe^{3+}/\Sigma Fe$ of each experiment. The discontinuous line is a linear fit of the data.

4.3 H_2O dependence

Dissolved H_2O in melt has already been demonstrated to strongly enhance diffusivities in silicate melts, both for major elements (e.g. Baker, 1991; Baker and Bossányi, 1994; González-García et al., 2017, 2019) and trace elements (Watson, 1981; Baker and Bossányi, 1994; Behrens and Zhang, 2001; Zhang et al., 2010; González-Garcia et al., 2018; Spallanzani et al., 2022). Our experimental dataset confirms this observation, and for the TP55 composition, major element diffusion is enhanced by 1.2-1.5 log units (corresponding to a factor of 20-30) when H_2O contents increase from 0.3 to 3.3 wt.% at 1250 °C. At 1200 °C, the enhancement factor amounts to 0.8-1.0 log units for an increase in H_2O content from 1.1 to 3.0 wt% H_2O (Figure 5). For the dataset obtained at 1150 °C, with two successful runs at 1.6 and 3 wt.% H_2O, the enhancement is in the order of 0.5 log units for all elements. Here, runs at different fO_2 were treated together, since oxygen fugacity is not expected to have major effects in diffusivity, except for Fe (see above).

Table 3: Parameters *a*, *b* and *c* obtained from fitting the H_2O-dependent diffusivities with an exponential law in the form log $D = a - b \cdot e^{c \cdot w}$. RMSE = root mean squere error.

Component	*a*	*b*	*c*	RMSE
		T = 1200 ºC		
Si	-10.84 ± 0.03	4.63 ± 0.42	-1.28 ± 0.10	0.017
Ti	-11.04 ± 0.26	2.76 ± 1.25	-0.94 ± 0.59	0.054
Al	-10.39 ± 0.03	4.48 ± 0.16	-1.23 ± 0.05	0.127
Mg	-10.63 ± 0.02	3.68 ± 0.11	-1.06 ± 0.05	0.022
Ca	-10.65 ± 0.01	4.34 ± 0.08	-1.19 ± 0.02	0.017
K	-10.60 ± 0.06	3.53 ± 0.52	-1.06 ± 0.17	0.116
		T = 1250 ºC		
Si	-10.77 ± 0.07	2.03 ± 0.16	-1.11 ± 0.18	0.038
Ti	-11.01 ± 0.13	1.89 ± 0.19	-1.19 ± 0.35	0.073
Al	-10.21 ± 0.16	1.97 ± 0.18	-0.94 ± 0.36	0.050
Mg	-10.59 ± 0.12	1.90 ± 0.19	-0.95 ± 0.24	0.053
Ca	-10.51 ± 0.20	2.00 ± 0.16	-0.95 ± 0.33	0.087
K	-10.49 ± 0.13	1.94 ± 0.19	-0.91 ± 0.24	0.056

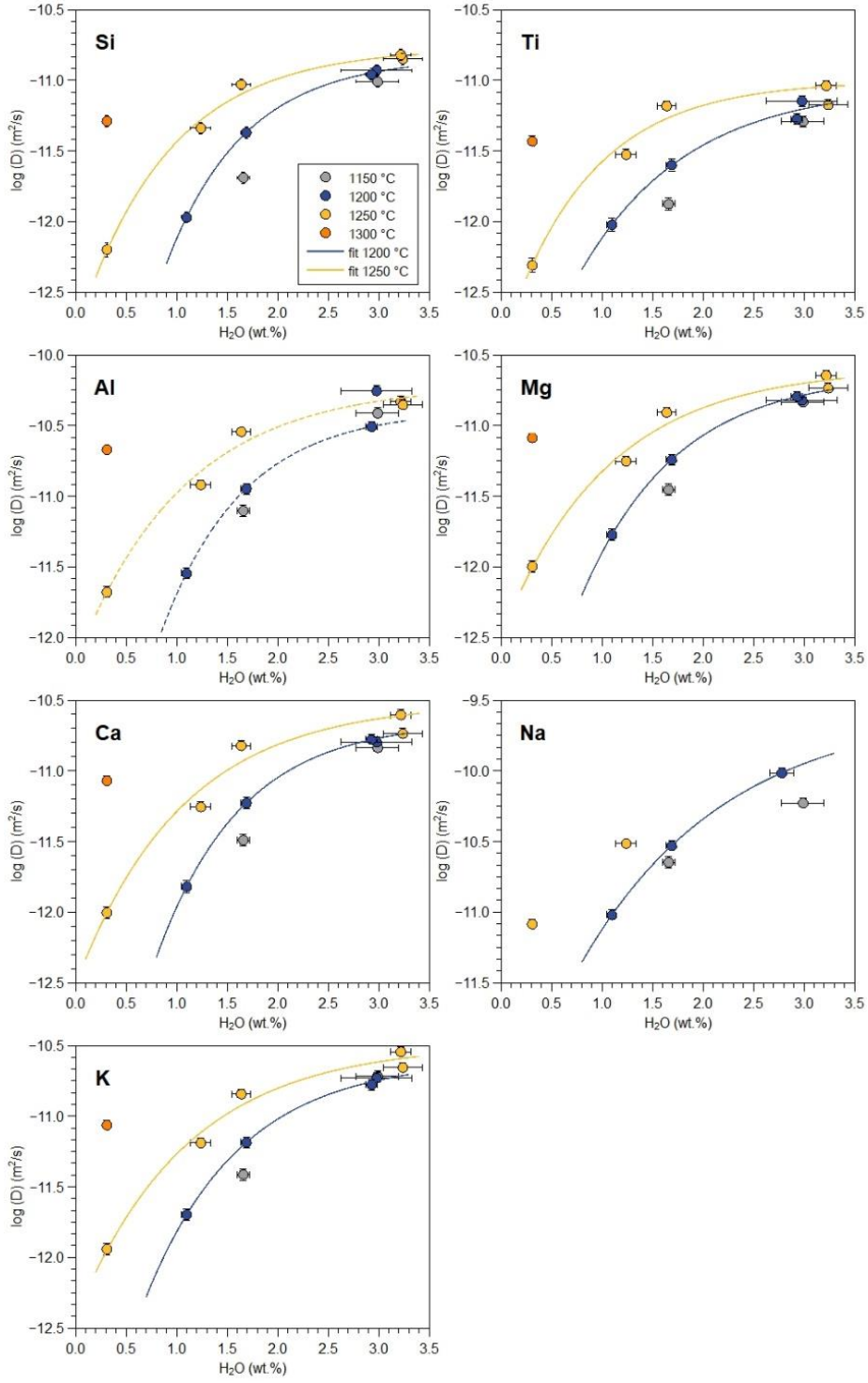

Figure 5: Water-dependence of major element effective binary diffusivities for a 55 wt.% SiO_2 compositional term.

Moreover, the increase in *D* as a function of H_2O in wt% is clearly non-linear, and instead it can be modelled by an exponential function in the form $\log D = a - b * e^{c*w}$, where *a*, *b* and *c* are fitting parameters, and *w* is H_2O concentration given in wt%. Parameter *a* gives the asymptotic log *D* value, i.e. the diffusivity at the saturation level. This fitting equation was applied to our diffusion datasets at 1200 ºC and 1250 °C, using an instrumentally weighted Levenberg-Marquadt least-squares algorithm in the software QtiPlot v. 1.0.0. Fitting parameters for each component are provided in Table 3. The 1200 °C dataset, spanning from 1.1 to 3.0 wt.% H_2O, can be fitted with a root mean square error (RMSE) between 0.02 to 0.13 log *D* units (with *D* in m^2/s). The 1250 ºC dataset, spanning from 0.3 to 3.2 wt.% H_2O, yielded an RMSE between 0.04 to 0.09 log *D* units.

Such strongly nonlinear H_2O-diffusion relationships are not uncommon in the literature (e.g. Baker, 1991; Watson, 1994; Baker et al., 2002; Zhang et al., 2010), but fitting equations are rarely provided. For small variations in H_2O contents (0.3-2 wt.%), González-García et al. (2017, 2018) found linear relationships for a both major and trace elements in shoshonite-rhyolite couples, but the inclusion of diffusivities at dry conditions seemed to make a square root function more appropriate (González-García et al., 2019).

It is remarkable to note the convergence of elemental diffusivities in both datasets towards high H_2O contents, which also includes the data point at 1150 °C and 3 wt.% H_2O. At such high H_2O concentrations, all experimentally measured diffusivities are within 0.4 log units, compared to a variation of 0.6-0,8 log units at 1,6 wt.% H_2O. A consequence of this behaviour is that the slowest components (in our case, Ti and Si) are subject of a greater enhancing effect by the addition of H_2O, confirming previous observations (e.g. Watson, 1994). The exponential dependence of *D* on H_2O contents is likely controlled by melt viscosity, which follows a similar non-linear evolution with H_2O contents. Our observation suggests that H_2O plays a major role in increasing the efficiency of chemical mixing in interacting melts, virtually equalizing diffusivity variations across a temperature range. Therefore, water-rich magmatic environments, such as those present in the Canary Islands, could be more susceptible to developing efficient mixing between melts than water-poor melts, not only diminishing the viscosity, but also reducing the viscosity difference between endmembers.

4.4 Arrhenius relations

The temperature dependence of diffusion is well established and is determined by the Arrhenius equation:

$$D = D_0 * e^{-E_a/RT} \quad (3)$$

where D_0 is the pre-exponential factor (m^2/s), E_a is the activation energy of the diffusion process (J/mol), *R* is the gas constant (J/mol·K) and *T* is temperature (K). By plotting 1000/*T* vs ln *D*, and fitting measured diffusivities with a linear regression, it is therefore possible to calculate D_0 and E_a and characterize the *T* dependence of major element diffusion. The dataset was fit using the same procedure and software detailed above for obtaining H_2O vs *D* equations.

From our experimental dataset, Arrhenius equations relating temperature and diffusivity were obtained at specific conditions. The major parameter influencing diffusion in our dataset is H_2O content, but its measured value varies up to 0.1-0.3 wt.% for

experiments with the same nominal H_2O content. Therefore, a correction of diffusion coefficients to a common H_2O concentration must be done before plotting the Arrhenius relations. We used the H_2O-dependent equations obtained in the previous section (Table 3) to obtain diffusivities at 1200 °C and 1250 °C for fixed H_2O contents of 1.66 and 2.99 wt.%. These values were determined by the H_2O contents of the experiments at 1150 °C, where an H_2O-dependent equation was not obtained.

Figure 6 shows Arrhenius fits for Si, Ti, Al, Mg, Ca and K, and the obtained parameters are summarized in Table 4. Fe is not included due to inconsistencies arising from the different $Fe^{3+}/\Sigma Fe$ ratios in experiments, and Na data is insufficient for obtaining Arrhenius parameters of good quality. Results show a coherent picture, indicating a decrease of E_a with increasing H_2O content from 220-290 kJ/mol at 1.66 wt.% H_2O to 47-112 kJ/mol at 2.99 wt% H_2O. Activation energies and ln D_0 for both H_2O concentrations plot to a single compensation law linear fit (Hart, 1981; Supplementary Figure 4). This is in line with previously published data, where H_2O contents are known to reduce activation energy of diffusion (Watson, 1981, 1994; Behrens and Zhang, 2001; Spallanzani et al., 2022). Only Al shows an anomalous behaviour, where the fitting errors are larger for the 1.66 wt.% fit, and the data at 1150°C and 2.99 wt.% H_2O does not allow to obtain a good Arrhenian fit.

Table 4. Arrhenius parameters calculated for 1.66 and 2.99 wt.% H_2O.

Component	ln D_0	E_a (kJ/mol)	R^2
	H_2O = 1.66 wt.%		
Si	-2.76 ± 0.89	286.8 ± 6.1	0.99
Ti	-2.71 ± 2.26	293.1 ± 3.3	0.99
Al	-6.39 ± 4.91	228.6 ± 60.0	0.94
Mg	-7.67 ± 2.06	222.4 ± 25.2	0.99
Ca	-3.91 ± 1.67	268.1 ± 20.4	0.99
K	-6.53 ± 1.87	234.9 ± 22.8	0.99
	H_2O = 2.99 wt.%		
Si	-18.71 ± 0.59	79.0 ± 7.8	0.99
Ti	-16.57 ± 1.37	112.2 ± 16.8	0.98
Al	-	-	-
Mg	-19.37 ± 0.59	66.5 ± 7.2	0.99
Ca	-16.59 ± 1.57	99.8 ± 19.2	0.96
K	-20.72 ± 3.63	47.8 ± 44.4	0.54

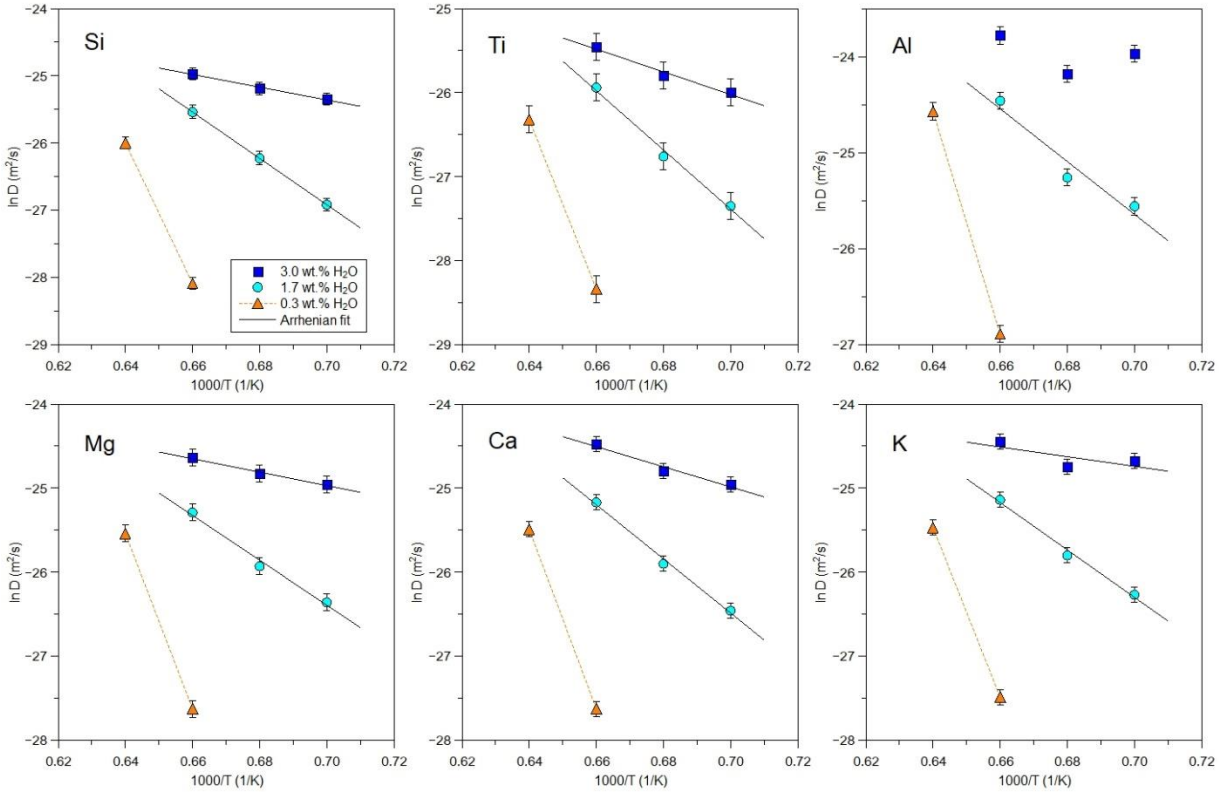

Figure 6: Arrhenius relations of TP55 for six major elements at 1.66 and 2.99 wt% H_2O. Although no equation was derived from the two data points at 0.3 wt%, their determined ln *D* values are plotted for reference.

4.5 The case of aluminium

Throughout our complete dataset, Al is the second fastest diffusing element after Na, and Al diffusivities are 0.4 log units faster than Si. This behaviour can be considered as anomalous, given that the expected network-forming character of Al^{3+} in the silicate network should result in diffusivities comparable to that of Si^{4+} and Ti^{3+}. A comparison of our Al diffusivities with published data (Figure 7) confirms this anomaly. Al diffusion in TP55 melt composition with 2.7 to 3.3 wt% H_2O plots between one and two orders of magnitude above diffusivities measured by Baker and Bossányi (1994) in wet dacite with the same range in H_2O content and is comparable to those observed in dry basalts and basanites at 1500 °C (Lundstrom, 2003; Chen and Zhang, 2008, 2009); i.e. 200 to 350 ºC warmer than our experimental conditions. This behaviour is not observed in Si, which shows diffusivities not differing strongly from literature data for a similar water contents. The comparison to Eyring diffusivity (i.e. viscosity-related diffusion, usually applied to network-forming cations; Glasstone et al. (1941)) of TP55 at different H_2O contents yields similar differences, with Al EBD plotting significantly above Eyring *D* values (Figure 7). Although Si data plot also above Eyring *D*, their deviations are lower and consistent with previous studies (Fanara et al., 2017). The large departure of Al from Eyring diffusivity is also contrasting to the comparatively low deviations observed by Fanara et al. (2017)

for trivalent cations. The only dataset supporting a high Al mobility in silicate melts comes from dynamic mixing experiments performed with K-series alkaline melts from Campi Flegrei. In such experiments, Perugini et al. (2013, 2015) showed that the relaxation of concentration variance (*R*, which is highly dependent on diffusivity) of Al is larger than most major components, falling between that of Na and K. On the other hand, this behaviour is not observed in chaotic mixing experiments with subalkaline melts (Morgavi et al., 2013), where Al mobility is similar to that of Si and Ti. Overall, these observations point to a fast Al diffusion mechanism operating in highly alkaline melts, in agreement with our diffusion experiments.

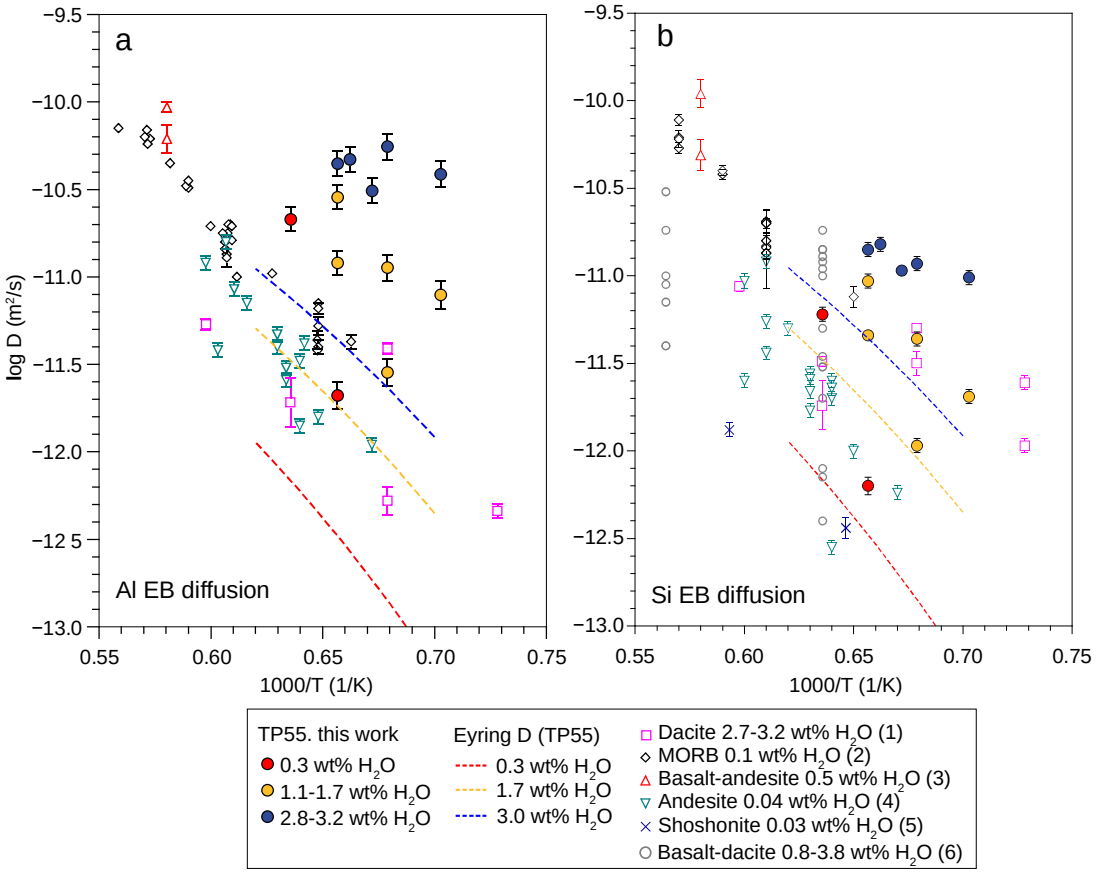

Figure 7: (a) Al and (b) Si effective binary (EB) diffusion data obtained in this work compared to bibliographic data. Dashed lines indicate Eyring diffusivity for TP55 at H_2O contents of 0.3, 1.7 and 3.0 wt.%, with viscosities calculated using the Giordano et al. (2008) model. Bibliographic data from: (1) Baker & Bossanyi (1994), (2) Chen et al. (2008), (3) Lundstrom (2003), (4) Zhang et al. (1989), (5) González-García et al. (2019), (6) Koyaguchi (1989).

In the silicate melt framework, Al usually plays the role of a network-former cation (Mysen et al., 1981), and as such its diffusivity is expected to be comparable to that of other network-former cations in tetrahedral coordination (Si, Ti) and to Eyring diffusivity. Departures from this behaviour have been suggested for high-P and peraluminous magmas, suggesting that

Al may not be in tetrahedral coordination if local charge balance is not attained with M^+ (Na, K) and M^{2+} (Ca) cations (Mysen et al., 1981). In molecular dynamics simulations, alkali cations (especially Na^+) tend to cluster around Al^{3+} to compensate charge balance (Le Losq et al., 2017), which could lead to increased Al diffusivity, where highly mobile Na cations result in an enhancement effect in Al mobility in the melt. This effect is greatly facilitated in melts with large Na/K ratio, while in K-rich melts the large size of K^+ promotes polymerization, with in turn increases diffusivities and viscosities.

A complementary explanation for the observed Al behaviour could potentially reside in multicomponent diffusion effects. Diffusion in a complex, multicomponent system is subject to diffusive coupling between oxides, usually resulting in uphill diffusion of one or more components (e.g. Guo and Zhang, 2016, 2018). This is the case for Al in basalt-rhyolite couples or other systems with similar endmembers (e.g. Koyaguchi, 1989; González-García et al., 2017), but Al uphill diffusion is notably absent in our tephrite-phonolite couples. This behaviour is however expected, since the occurrence of uphill diffusion is highly dependent on the arrangement of end-members in the compositional space, as observed in simple, three-component systems (Chakraborty et al., 1995b).

Multicomponent diffusion experiments in the system K_2O-Al_2O_3-SiO_2, (Chakraborty et al., 1995a,b) suggest again that Al diffusion is coupled to alkalis. The degree of coupling depends on composition (peralkaline vs peraluminous) and the nature of the gradient of all remaining elements. In our system, an indication of Al-K diffusive coupling comes from their behaviour in the Arrhenius plots (Figure 6). Al and K show here an anomalous behaviour, both deviating from linearity. Diffusivities of Al and K show an increase from 1200 to 1150°C, especially evident in the 3.0 wt% H_2O data. This behaviour could potentially be related to a change in the Al-K diffusive coupling at lower temperatures due to the variation of the intrinsic diffusivity of both elements.

4.6 Implications for magma mixing in Tenerife

The experimental results obtained in this work can be used to obtain some insights on the petrogenesis of bimodal ignimbrite sheets in the Diego Hernández Formation of Tenerife. In several of these units, the presence of banded pumices suggests the occurrence of a magma mixing event shortly before the eruption (González-García et al., 2022). During magma mixing, the combined effects of diffusion and advection progressively reduce the compositional variability of the system and tend to produce a hybrid composition. Perugini et al. (2015) proposed that the concentration variance normalized to that of the starting endmembers (σ_n^2) of elemental concentrations in the mixing melts is reduced with time, following an exponential decay function with a decay parameter *R* that depends, among other parameters, on the diffusion rate of the considered element. In consequence, in systems where magma mixing is the primary process controlling compositional variability, σ_n^2 can be used as a measure of the chemical hybridization of the system.

Here we use compositions of groundmass glass in three banded pumices clasts from the El Abrigo ignimbrite, Tenerife (González-García et al., 2022), to obtain the values of σ_n^2 for Si, Ti, Al, Fe, Mg, Na and K. Concentration variance was normalized using the compositions of the two endmember melts proposed by González-García et al. (2022), i.e., a phonotephrite represented by the most mafic glass in banded pumices, and a high-Zr phonolite from aphyric white pumices.

The obtained σ_n^2 values were later compared to diffusivities obtained in run DCB-11 (1200ºC, 2.93 wt% H_2O). The choice of this experiment for comparison is based on the availability of Na diffusivities and its high H_2O content, close to that expected for the phonolitic melt of the El Abrigo ignimbrite, but analogous results are obtained using any other experiment. However, we should note that experimental temperatures are still 150-200ºC higher than expected for the natural system.

The results (Figure 8) show a correlation between diffusion coefficients and σ_n^2, with slow diffusing elements showing a lesser homogenization than fast-diffusing elements (mainly Na). These data confirms that the main control of melt chemistry in the banded pumices is the diffusive exchange between endmembers. However, two outliers are present in Al and K, which in turn could provide additional insight on the issue of Al diffusivity. Figure 8 shows that σ_n^2 in the mixed eruption products does not correlate to the fast Al diffusivity measured in our experiments, but instead suggests a slow diffusion mechanism in the natural system. In one of the banded pumices, K follows a similar behavior, with one of the σ_n^2 value higher than expected from its measured diffusivity. A potential explanation for this behavior could be in the variable degree of Al-alkalis coupling with varying temperature. The experimental results from this work and from Perugini et al. (2013), where high Al mobility is observed, were carried out at temperature between 1150 and 1300ºC. However, mixing temperatures in the El Abrigo system were significantly lower, likely in the range 900-1050ºC (González-García et al., 2022). A variation of the structural behaviour of Al towards a network former role at such low temperatures, favouring a slow Al diffusion mechanism similar to that observed in the literature, could potentially explain this divergence.

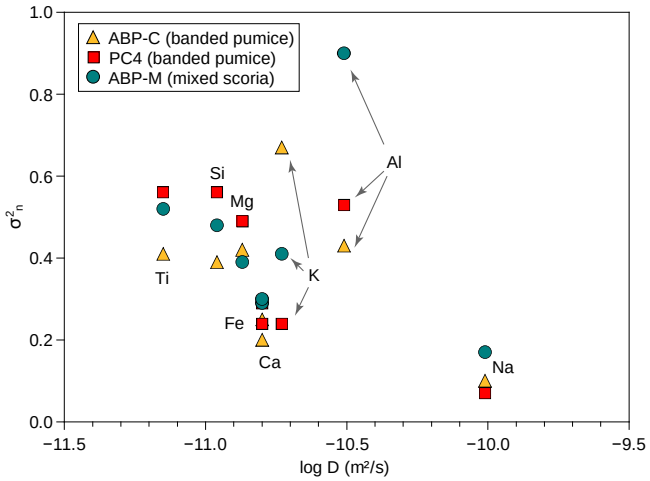

Figure 8: Comparison between experimental diffusivities for TP55 composition and normalized concentration variance (σ_n^2) for three mixed clasts form the El Abrigo ignimbrite. Plotted diffusivities are those from experiment DCB-11 (1200ºC, 2.93 wt% H_2O).

Alternatively, the reasons for this behavior could reside in crystal dissolution and assimilation processes in the natural products. The banded pumices in the El Abrigo deposit are mostly crystal-rich, with two coexisting mineral assemblages in disequilibrium. The melting and assimilation of enough quantities of alkali feldspar could potentially result in Al-K

inhomogeneities, which would increase their concentration variance relative to a mixing-only scenario. However, our current dataset does not allow us to distinguish between these two possible scenarios, and more experimental data at lower temperature would be necessary to confirm the occurrence of a varying diffusive mechanism for Al.

5 Conclusions

Diffusion coefficients of major elements have been obtained from tephrite-phonolite couples with compositions relevant for Canary Islands magmatism. Diffusivities show a wide variation range, with Na and Al being significantly faster (ca. 0.5 and 1 log unit, respectively) than Si. All log *D* values for an intermediate composition (55 wt.% SiO_2) have a strongly non-linear relationship with dissolved H_2O, which is best adjusted by an exponential expression. In addition, an apparent convergence of diffusivities is evident towards the water-rich end (3 wt.%) of our dataset, which suggests that the addition of H_2O could increase magma mixing efficiency by equalizing major element diffusivities. Arrhenius equations obtained at 1.66 and 2.99 wt% are also convergent with increasing temperature, and E_a values decrease with H_2O contents. The anomalous behaviour of Al, which is second in diffusivity only after Na, may be explained by a change of behaviour from network-forming to network-modifying cation by complexation with Na^+ and K^+ cations. Such behaviour may be a common occurrence in highly alkaline melts. This result suggests the occurrence of a fast diffusion mechanism for Al in our experimental dataset, different to that observed in the literature.

Our results may have important implications in the study of kinetic processes in highly alkaline magmas, and particularly melt hybridization during magma mixing events. The comparison of our experimental results with the chemical distribution in mixed pyroclasts from the El Abrigo ignimbrite confirms that diffusion is the main mechanism controlling the chemical variability in the melt phase. However, the natural Al distribution does not support the fast Al diffusion mechanism observed in the experiment. We suggest that at the low temperatures inferred for the mixing event (900-1050 ºC), Al does not show the fast diffusivities observed in experiments, likely due to a change in coupling to Na^+ and K^+. Alternatively, this could be an effect of melting and assimilation of a K-feldspar rich mush, which is documented at the El Abrigo eruption.

Acknowledgements

This research was funded by an Alexander von Humboldt Postdoctoral Fellowship of the Alexander von Humboldt Foundation to D.G.-G. Phillipp Beckmann and Philip Wiegel are acknowledged for assistance during experiment run and EPMA analysis, respectively, and Julian Hübner for Fe determination in experimental glasses. F.M., F.P., F.H. and R.A. acknowledge support provided by DFG Research Unit 2881 (Diffusion Chronometry). Harald Behrens and Sumit Chakraborty are acknowledged for assistance in data interpretation and comments of an early version of this manuscript.

References

Ablay, G. J., Carroll, M. R., Palmer, M. R., Marti, J., and Sparks, R. S. J.: Basanite–Phonolite Lineages of the Teide–Pico Viejo Volcanic Complex, Tenerife, Canary Islands, J. Petrol., 39, 905–936, 1998.

Andújar, J. and Scaillet, B.: Experimental Constraints on Parameters Controlling the Difference in the Eruptive Dynamics of Phonolitic Magmas: the Case of Tenerife (Canary Islands), J. Petrol., 53, 1777–1806, doi:10.1093/petrology/egs033, 2012.

Andújar, J., Costa, F., Martí, J., Wolff, J. A., and Carroll, M. R.: Experimental constraints on pre-eruptive conditions of phonolitic magma from the caldera-forming El Abrigo eruption, Tenerife (Canary Islands), Chem. Geol., 257, 173–191, doi: 10.1016/j.chemgeo.2008.08.012, 2008.

Andújar, J., Costa, F., and Martí, J.: Magma storage conditions of the last eruption of Teide volcano (Canary Islands, Spain), B. Volcanol., 72, 381–395, doi: 10.1007/s00445-009-0325-3, 2010.

Baker, D. R.: Tracer versus trace element diffusion: Diffusional decoupling of Sr concentration from Sr isotope composition, Geochimica et Cosmochimica Acta, 53, 3015–3023, https://doi.org/10.1016/0016-7037(89)90177-4, 1989.

Baker, D. R.: Interdiffusion of hydrous dacitic and rhyolitic melts and the efficacy of rhyolite contamination of dacitic enclaves, Contr. Mineral. and Petrol., 106, 462–473, https://doi.org/10.1007/BF00321988, 1991.

Baker, D. R.: Interdiffusion of hydrous dacitic and rhyolitic melts and the efficacy of rhyolite contamination of dacitic enclaves, Contr. Mineral. Petrol., 106, 462–473, doi:10.1007/BF00321988, 1991.

Baker, D. R. and Bossányi, H.: The combined effect of F and H_2O on interdiffusion between peraikaline dacitic and rhyolitic melts, Contrib. Mineral. Petrol., 117, 203–214, 1994.

Baker, D. R., Conte, A., Freda, C., and Ottolini, L.: The effect of halogens on Zr diffusion and zircon dissolution in hydrous metaluminous granitic melts, Contrib. Mineral. Petrol., 142, 666–678, doi:10.1007/s00410-001-0328-3, 2002.

Behrens, H.: Determination of water solubilities in high-viscosity melts: An experimental study on NaAlSi3O8 and KAlSi3O8 melts. Eur. J. Mineral., 7, 905-320, 1995.

Behrens, H., Romano, C., Nowak, M., Holtz, F., and Dingwell, D. B.: Near-infrared spectroscopic determination of water species in glasses of the system MAlSi3O8 (M = Li, Na, K) : an interlaboratory study, Chemical Geology, 128, 41–63, https://doi.org/10.1016/0009-2541(95)00162-X, 1996.

Behrens, H. and Zhang, Y.: Ar diffusion in hydrous silicic melts: implications for volatile diffusion mechanisms and fractionation, Earth Planet. Sc. Lett., 192, 363–376, doi: 10.1016/S0012-821X(01)00458-7, 2001.

Berndt, J., Liebske, C., Holtz, F., Freise, M., Nowak, M., Ziegenbein, D., Hurkuck, W., and Koepke, J.: A combined rapid-quench and H_2-membrane setup for internally heated pressure vessels: Description and application for water solubility in basaltic melts, Am. Mineral., 87, 1717–1726, doi:10.2138/am-2002-11-1222, 2002.

Berthod, C., Médard, E., Di Muro, A., Hassen Ali, T., Gurioli, L., Chauvel, C., Komorowski, J.-C., Bachèlery, P., Peltier, A., Benbakkar, M., Devidal, J.-L., Besson, P., Le Friant, A., Deplus, C., Nowak, S., Thinon, I., Burckel, P., Hidalgo, S., Feuillet, N., Jorry, S., and Fouquet, Y.: Mantle xenolith-bearing phonolites and basanites feed the active volcanic ridge of

Mayotte (Comoros archipelago, SW Indian Ocean), Contrib. Mineral. Petrol., 176, 75, doi:10.1007/s00410-021-01833-1, 2021.

Bouhifd, M. A., Whittington. A. G. and Richet, P.: Densities and volumes of hydrous silicate melts: New measurements and predictions. Chem. Geol. 418, 40-50, doi: 10.1016/j.chemgeo.2015.01.012, 20115.

Bryan, S. E., Martí, J., and Leosson, M.: Petrology and Geochemistry of the Bandas del Sur Formation, Las Cañadas Edifice, Tenerife (Canary Islands), J. Petrol., 43, 1815–1856, doi:10.1093/petrology/43.10.1815, 2002.

Carroll, M. R. and Blank, J. G.: The solubility of H_2O in phonolitic melts, Am. Mineral., 82, 549–556, doi:10.2138/am-1997-5-615, 1997.

Chakraborty, S., Dingwell, D. B., and Rubie, D. C.: Multicomponent diffusion in ternary silicate melts in the system K_2O-Al_2O_3-SiO_2: I. Experimental measurements, Geochim. Cosmochim. Ac., 59, 255–264, doi:10.1016/0016-7037(94)00283-R, 1995a.

Chakraborty, S., Dingwell, D. B., and Rubie, D. C.: Multicomponent diffusion in ternary silicate melts in the system K_2O-Al_2O_3-SiO_2: II. Mechanisms, systematics, and geological applications, Geochim. Cosmochim. Ac., 59, 265–277, 1995b.

Chen, Y. and Zhang, Y.: Olivine dissolution in basaltic melt, Geochim. Cosmochim. Ac., 72, 4756–4777, doi:10.1016/j.gca.2008.07.014, 2008.

Chen, Y. and Zhang, Y.: Clinopyroxene dissolution in basaltic melt, Geochim. Cosmochim. Ac., 73, 5730–5747, doi:10.1016/j.gca.2009.06.016, 2009.

De Campos, C. P., Perugini, D., Ertel-Ingrisch, W., Dingwell, D. B., and Poli, G.: Enhancement of magma mixing efficiency by chaotic dynamics: an experimental study, Contrib. Mineral. Petrol., 161, 863–881, do:10.1007/s00410-010-0569-0, 2011.

DeVitre, C. L., Gazel, E., Allison, C. M., Soto, G., Madrigal, P., Alvarado, G. E., and Lücke, O. H.: Multi-stage chaotic magma mixing at Turrialba volcano, J. Volcanol. Geotherm. Res., 381, 330–346, doi:10.1016/j.jvolgeores.2019.06.011, 2019.

Dingwell, D. B., Romano, C., and Hess, K.-U.: The effect of water on the viscosity of a haplogranitic melt under P-T-X conditions relevant to silicic volcanism, Contrib. Mineral. Petrol., 124, 19–28, doi:10.1007/s004100050170, 1996.

Dorado, O., Andújar, J., Martí, J., and Geyer, A.: Pre-eruptive conditions at satellite vent eruptions at Teide-Pico Viejo complex (Tenerife, Canary Islands), Lithos, 396–397, 106193, doi:10.1016/j.lithos.2021.106193, 2021.

Fanara, S., Sengupta, P., Becker, H.-W., Rogalla, D., and Chakraborty, S.: Diffusion across the glass transition in silicate melts: Systematic correlations, new experimental data for Sr and Ba in calcium-aluminosilicate glasses and general mechanisms of ionic transport, J. Non-Cryst. Solids, 455, 6–16, doi:10.1016/j.jnoncrysol.2016.10.013, 2017.

Fuchs, P.: Petrogenesis of basanite-phonolite series of an oceanic intraplate volcano: combining experimental data and field observations, PhD thesis, Leibniz Universität Hannover, 182 pp., doi:10.15488/8253, 2014.

Ghiorso, M. S. and Gualda, G. A. R.: An H_2O–CO_2 mixed fluid saturation model compatible with rhyolite-MELTS, Contrib. Mineral. Petrol., 169, 53, doi:10.1007/s00410-015-1141-8, 2015.

Giordano, D. and Dingwell, D.: Viscosity of hydrous Etna basalt: implications for Plinian-style basaltic eruptions, B. Volcanol, 65, 8–14, doi:10.1007/s00445-002-0233-2, 2003.

Glasstone, S., Laider, K. J., and Eyring, H.: The Theory of Rate Processes, McGraw-Hill, New York, 1941.

González-García, D., Behrens, H., Petrelli, M., Vetere, F., Morgavi, D., Zhang, C., and Perugini, D.: Water-enhanced interdiffusion of major elements between natural shoshonite and high-K rhyolite melts, Chem. Geol., 466, 86–101, doi:10.1016/j.chemgeo.2017.05.023, 2017.

González-Garcia, D., Petrelli, M., Behrens, H., Vetere, F., Fischer, L. A., Morgavi, D., and Perugini, D.: Diffusive exchange of trace elements between alkaline melts: Implications for element fractionation and timescale estimations during magma mixing, Geochim. Cosmochim. Ac., 233, 95–114, doi:10.1016/j.gca.2018.05.003, 2018.

González-García, D., Vetere, F., Behrens, H., Petrelli, M., Morgavi, D., and Perugini, D.: Interdiffusion of major elements at 1 atmosphere between natural shoshonitic and rhyolitic melts, Am. Mineral., 104, 1444–1454, doi.:10.2138/am-2019-6997, 2019.

González-García, D., Petrelli, M., Perugini, D., Giordano, D., Vasseur, J., Paredes-Mariño, J., Marti, J., and Dingwell, D. B.: Pre-eruptive conditions and dynamics recorded in banded pumices from the El Abrigo caldera-forming eruption (Tenerife, Canary Islands), J. Petrol., 63, egac009, doi:10.1093/petrology/egac009, 2022.

González-García, D., Boulesteix, T., Klügel, A., and Holtz, F.: Bubble-enhanced basanite–tephrite mixing in the early stages of the Cumbre Vieja 2021 eruption, La Palma, Canary Islands, Sci Rep, 13, 14839, doi:10.1038/s41598-023-41595-3, 2023.

Guo, C. and Zhang, Y.: Multicomponent diffusion in silicate melts: SiO_2–TiO_2–Al_2O_3–MgO–CaO–Na_2O–K_2O System, Geochim. Cosmochim. Ac., 195, 126–141, doi:10.1016/j.gca.2016.09.003, 2016.

Guo, C. and Zhang, Y.: Multicomponent diffusion in basaltic melts at 1350 °C, Geochim. Cosmochim. Ac., 228, 190–204, doi:10.1016/j.gca.2018.02.043, 2018.

Hart, S. R.: Diffusion compensation in natural silicates. Geochim. Cosmochim. Acta, 45(3), 279–291, doi:10.1016/0016-7037(81)90239-8, 1981.

Helz, R. T., Clague, D. A., Mastin, L. G., and Rose, T. R.: Electron Microprobe analyses of glasses from Kilauea tephra units, Kilauea volcano, Hawaii, USGS, 2014.

Jarosewich, E., Nelen, J. A., and Norberg, J. A.: Reference Samples for Electron Microprobe Analysis, Geostandard. Newslett., 4, 43–47, https://doi.org/10.1111/j.1751-908X.1980.tb00273.x, 1980.

Johansen, T. S., Hauff, F., Hoernle, K., Klügel, A., and Kokfelt, T. F.: Basanite to phonolite differentiation within 1550–1750 yr: U-Th-Ra isotopic evidence from the A.D. 1585 eruption on La Palma, Canary Islands, Geology, 33, 897, doi:10.1130/G21663.1, 2005.

Klügel, A., Hoernle, K. A., Schmincke, H.-U., and White, J. D. L.: The chemically zoned 1949 eruption on La Palma (Canary Islands): Petrologic evolution and magma supply dynamics of a rift zone eruption, J. Geophys. Res., 105, 5997–6016, doi:10.1029/1999JB900334, 2000.

Klügel, A., Hansteen, T. H., and Galipp, K.: Magma storage and underplating beneath Cumbre Vieja volcano, La Palma (Canary Islands), Earth Planet. Sc. Lett., 236, 211–226, doi:10.1016/j.epsl.2005.04.006, 2005.

Klügel, A., Albers, E., and Hansteen, T. H.: Mantle and Crustal Xenoliths in a Tephriphonolite From La Palma (Canary Islands): Implications for Phonolite Formation at Oceanic Island Volcanoes, Front. Earth Sci., 10, doi: 10.3389/feart.2022.761902 2022.

Koepke, J. and Behrens, H.: Trace element diffusion in andesitic melts: an application of synchrotron X-ray fluorescence analysis, Geochim. Cosmochim. Ac., 65, 1481–1498, doi:10.1016/S0016-7037(01)00550-6, 2001.

Koyaguchi, T.: Chemical gradient at diffusive interfaces in magma chambers, Contr. Mineral. and Petrol., 103, 143–152, doi:10.1007/BF00378500, 1989.

Le Losq, C., Neuville, D. R., Chen, W., Florian, P., Massiot, D., Zhou, Z., and Greaves, G. N.: Percolation channels: a universal idea to describe the atomic structure and dynamics of glasses and melts, Sci. Rep., 7, 16490, doi:10.1038/s41598-017-16741-3, 2017.

Le Losq, C., Valentine, A. P., Mysen, B. O., and Neuville, D. R.: Structure and properties of alkali aluminosilicate glasses and melts: Insights from deep learning, Geochim. Cosmochim. Ac., 314, 27–54, doi:10.1016/j.gca.2021.08.023, 2021.

Liang, Y.: Multicomponent Diffusion in Molten Silicates: Theory, Experiments, and Geological Applications, Rev. Mineral. and Geochem., 72, 409–446, doi:10.2138/rmg.2010.72.9, 2010.

Lundstrom, C. C.: An experimental investigation of the diffusive infiltration of alkalis into partially molten peridotite: Implications for mantle melting processes, Geochem. Geophys. Geosyst., 4, 8614, doi:10.1029/2001GC000224, 2003.

Mangler, M. F., Humphreys, M. C. S., Geifman, E., Iveson, A. A., Wadsworth, F. B., Brooker, R. A., Lindoo, A., and Hammond, K.: Melt Diffusion-Moderated Crystal Growth and its Effect on Euhedral Crystal Shapes, J. Petrol., 64, egad054, doi:10.1093/petrology/egad054, 2023.

Martí, J., Zafrilla, S., Andújar, J., Jiménez-Mejías, M., Scaillet, B., Pedrazzi, D., Doronzo, D., and Scaillet, S.: Controls of magma chamber zonation on eruption dynamics and deposits stratigraphy: The case of El Palomar fallout succession (Tenerife, Canary Islands), J. Volcanol. Geotherm. Res., 399, 106908, doi:10.1016/j.jvolgeores.2020.106908, 2020.

Marxer, F. and Ulmer, P.: Crystallisation and zircon saturation of calc-alkaline tonalite from the Adamello Batholith at upper crustal conditions: an experimental study, Contrib Mineral Petrol, 174, 84, doi:10.1007/s00410-019-1619-x, 2019.

Morgavi, D., Perugini, D., De Campos, C. P., Ertl-Ingrisch, W., Lavallée, Y., Morgan, L., and Dingwell, D. B.: Interactions between rhyolitic and basaltic melts unraveled by chaotic mixing experiments, Chem. Geol., 346, 199–212, doi:10.1016/j.chemgeo.2012.10.003, 2013.

Mysen, B. O., Virgo, D., and Kushiro, I.: The structural role of aluminum in silicate melts—a Raman spectroscopic study at 1 atmosphere, Am. Mineral., 66, 678–701, 1981.

Nowak, M. and Behrens, H.: An experimental investigation on diffusion of water in haplogranitic melts, Contrib Mineral Petrol, 126, 365–376, https://doi.org/10.1007/s004100050256, 1997.

Oliphant, T. E.: Python for Scientific Computing, Comput. Sci. Eng., 9, 10–20, doi:10.1109/MCSE.2007.58, 2007.

Paisley, R., Berlo, K., Whattam, J., Schipper, C. I., and Tuffen, H.: Degassing-induced chemical heterogeneity at the 2011-2012 Cordón Caulle eruption, Volcanica, 2, 211–237, doi:10.30909/vol.02.02.211237, 2019.

Pankhurst, M. J., Scarrow, J. H., Barbee, O. A., Hickey, J., Coldwell, B. C., Rollinson, G. K., Rodríguez-Losada, J. A., Lorenzo, A. M., Rodríguez, F., Hernández, W., Fernández, D. C., Hernández, P. A., and Pérez, N. M.: Rapid response petrology for the opening eruptive phase of the 2021 Cumbre Vieja eruption, La Palma, Canary Islands, Volcanica, 5, 1–10, doi:10.30909/vol.05.01.0110, 2022.

Perugini, D., Poli, G., Petrelli, M., De Campos, C. P., and Dingwell, D. B.: Time-scales of recent Phlegrean Fields eruptions inferred from the application of a 'diffusive fractionation' model of trace elements, B. Volcanol, 72, 431–447, doi:10.1007/s00445-009-0329-z, 2010.

Perugini, D., De Campos, C. P., Dingwell, D. B., and Dorfman, A.: Relaxation of concentration variance: A new tool to measure chemical element mobility during mixing of magmas, Chem. Geol., 335, 8–23, doi:10.1016/j.chemgeo.2012.10.050, 2013.

Perugini, D., De Campos, C. P., Petrelli, M., and Dingwell, D. B.: Concentration variance decay during magma mixing: a volcanic chronometer, Sci Rep, 5, 14225, doi:10.1038/srep14225, 2015.

Romano, C., Giordano, D., Papale, P., Mincione, V., Dingwell, D. B., and Rosi, M.: The dry and hydrous viscosities of alkaline melts from Vesuvius and Phlegrean Fields, Chem. Geol., 202, 23–38, doi:10.1016/S0009-2541(03)00208-0, 2003.

Sauer, F. and Freise, V.: Diffusion in binären Gemischen mit Volumenänderung, Z. Elektrochem., 66, 353–362, 1962.

Schuessler, J. A., Botcharnikov, R. E., Behrens, H., Misiti, V., and Freda, C.: Oxidation state of iron in hydrous phono-tephritic melts, Am. Mineral., 93, 1493–1504, doi:10.2138/am.2008.2795, 2008.

Shamloo, H. I. and Grunder, A. L.: Magma mingling and ascent in the minutes to hours before an explosive eruption as recorded by banded pumice, Geology, 51, 957–961, doi:10.1130/G51318.1, 2023.

Sliwinski, J. T., Bachmann, O., Ellis, B. S., Dávila-Harris, P., Nelson, B. K., and Dufek, J.: Eruption of Shallow Crystal Cumulates during Explosive Phonolitic Eruptions on Tenerife, Canary Islands, J. Petrol., 56, 2173–2194, doi:10.1093/petrology/egv068, 2015.

Spallanzani, R., Koga, K. T., Cichy, S. B., Wiedenbeck, M., Schmidt, B. C., Oelze, M., and Wilke, M.: Lithium and boron diffusivity and isotopic fractionation in hydrated rhyolitic melts, Contrib. Mineral. Petrol., 177, 74, doi:10.1007/s00410-022-01937-2, 2022.

Stolper, E.: Water in silicate glasses: An infrared spectroscopic study, Contrib. Mineral. Petrol., 81, 1–17, doi:10.1007/BF00371154, 1982.

Taylor, J. R., Wall, V. J., and Pownceby, M. I.: The calibration and application of accurate redox sensors, Am. Mineral., 77, 284–295, 1992.

Tomlinson, E. L., Smith, V. C., and Menzies, M. A.: Chemical zoning and open system processes in the Laacher See magmatic system, Contrib. Mineral. Petrol., 175, 19, doi:10.1007/s00410-020-1657-4, 2020.

Vetere, F., Botcharnikov, R. E., Holtz, F., Behrens, H., and De Rosa, R.: Solubility of H_2O and CO_2 in shoshonitic melts at 1250°C and pressures from 50 to 400 MPa: Implications for Campi Flegrei magmatic systems, J. Volcanol. Geotherm. Res., 202, 251–261, doi:10.1016/j.jvolgeores.2011.03.002, 2011.

Watson, E. B.: Diffusion in magmas at depth in the Earth: The effects of pressure and dissolved H_2O, Earth Planet. Sc. Lett., 52, 291–301, doi:10.1016/0012-821X(81)90184-9, 1981.

Watson, E.B.: Diffusion in Volatile-bearing Magmas. Rev. Mineral. Geochem., 30, 371-411, doi: 10.1515/9781501509674-016, 1994.

Wolff, J. A.: Zonation, mixing and eruption of silica-undersaturated alkaline magma: a case study from Tenerife, Canary Islands, Geol. Mag., 122, 623–640, doi:10.1017/S0016756800032039, 1985.

Zhang, Y. and Behrens, H.: H_2O diffusion in rhyolitic melts and glasses, Chem. Geol., 169, 243–262, doi.org/10.1016/S0009-2541(99)00231-4, 2000.

Zhang, Y. and Gan, T.: Diffusion in Melts and Magmas, Rev. Mineral. Geochem., 87, 283–337, doi:10.2138/rmg.2022.87.07, 2022.

Zhang, Y., Walker, D., and Lesher, C. E.: Diffusive crystal dissolution, Contr. Mineral. and Petrol., 102, 492–513, doi:10.1007/BF00371090, 1989.

Zhang, Y., Ni, H., and Chen, Y.: Diffusion Data in Silicate Melts, Rev. Mineral. Geochem., 72, 311–408, doi:10.2138/rmg.2010.72.8, 2010.

Chemical interdiffusion between Na-tephritic and phonolitic melts at different T, H_2O and fO_2

Diego González-García[1,2], Florian Pohl[1], Felix Marxer[1], Stepan Krasheninnikov[1,3], Renat Almeev[1], François Holtz[1]

[1]Institut für Mineralogie, Leibniz Universität Hannover, 30167 Hannover, Germany
[2]Current affiliation: Department of Mineralogy and Petrology, Universidad Complutense de Madrid, 28040 Madrid, Spain
[3]Institut für Geowissenschaften, Johannes Gutenberg Universität Mainz, 55128 Mainz, Germany

Correspondence to: Diego González-García (d.gonzalez-garcia@outlook.es)

SUPPLEMENTARY FIGURES

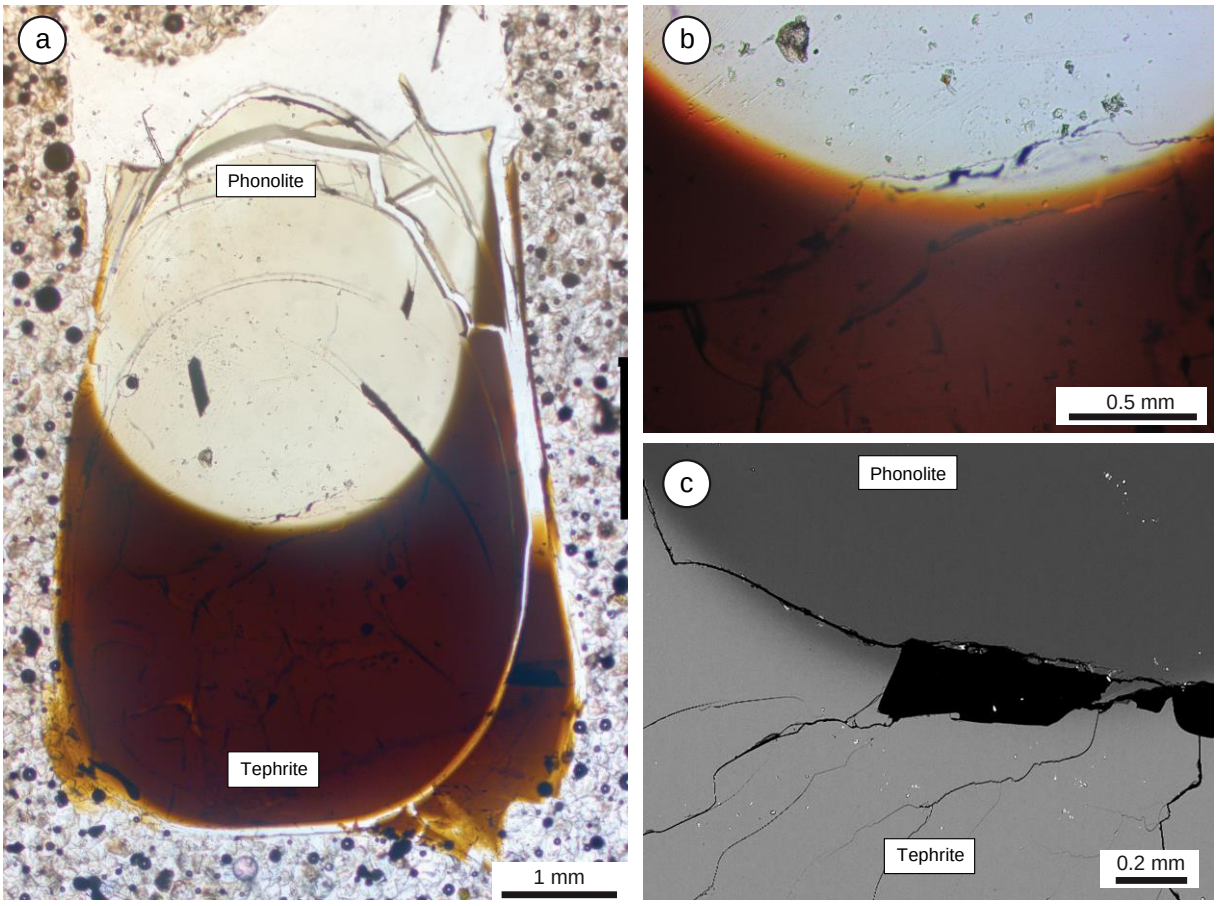

Supplementary figure 1. Zero-time experiment (DCB-01; 1200 ºC, 0.3 wt% H_2O), run to check for dissolution quench crystals in the tephritic melt during experiment heat-up. (a) Transmitted light whole-run mosaic; (b) detail of the interface in transmitted light and (c) back-scattered electron (BSE) image from the electron microprobe.

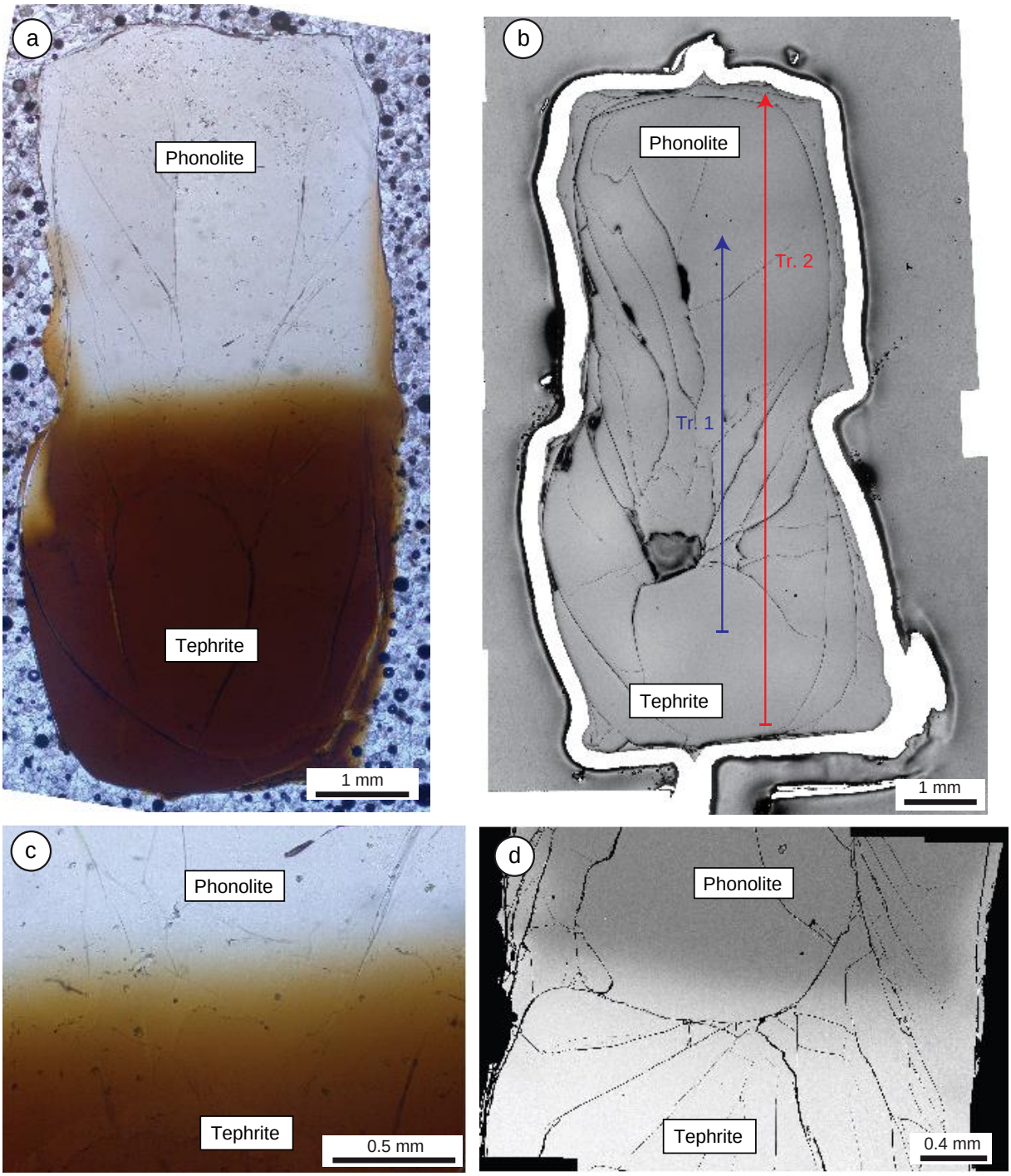

Supplementary figure 2. Example of a diffusion couple experiment. (a) Whole-run transmitted light mosaic form a double polished section (experiment DC-05); (b) reflected light mosaic of the same experiment mounted in epoxy, showing the approximate position of the short (Tr. 1) and long (Tr. 2) transects measured by the EPMA; (c) detail fo the interface of the same experiment in transmitted light; and (d) BSE mosaic of the interface region of experiment DCB-02.

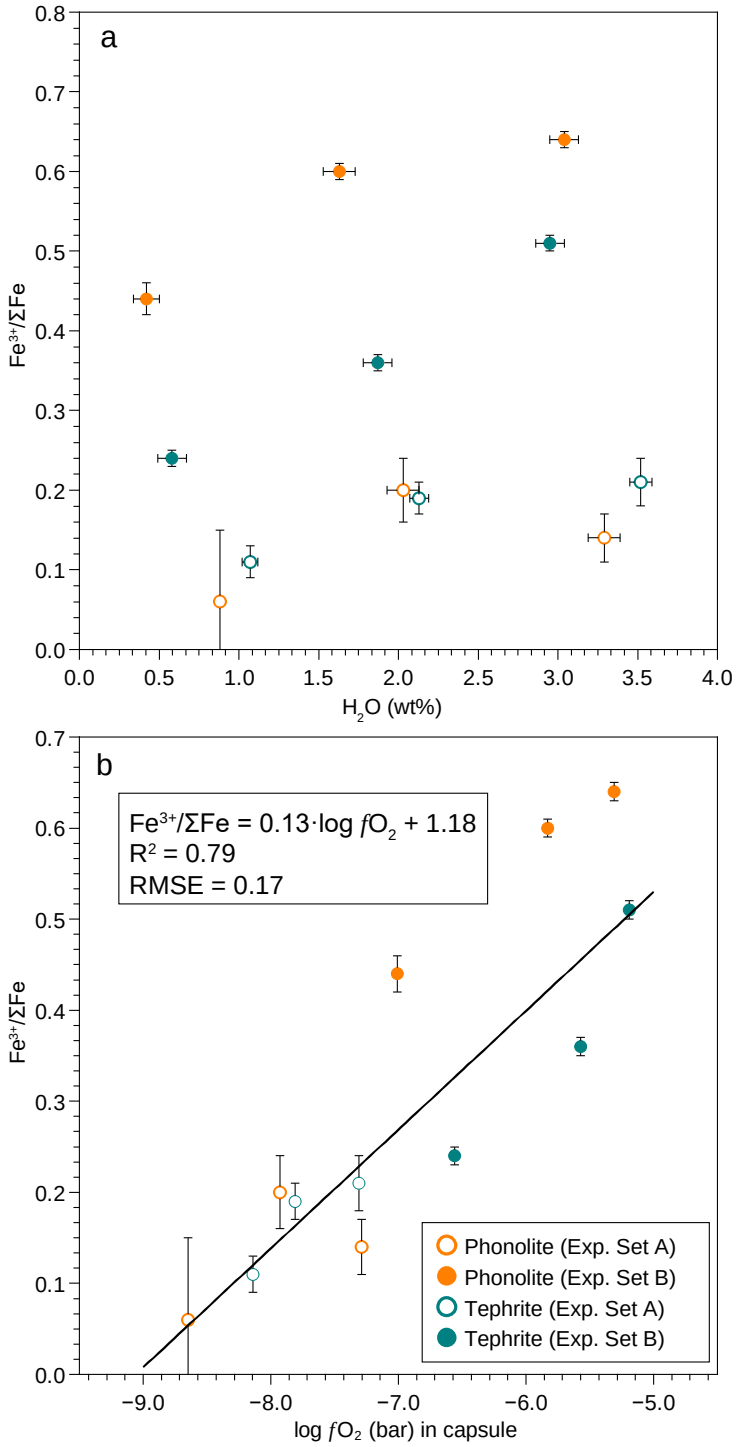

Supplementary figure 3. (a) Oxidation state of iron expressed as $Fe^{3+}/\Sigma Fe$ as a function of H_2O contents in synthesis runs, measured by wet chemistry (Schuessler et al. 2008) and Karl-Fischer Titration. Most data points are the average of two measurements. (b) Fe oxidation state as a function of estimated log fO_2 in capsule (see text for details), fitted by a linear function.

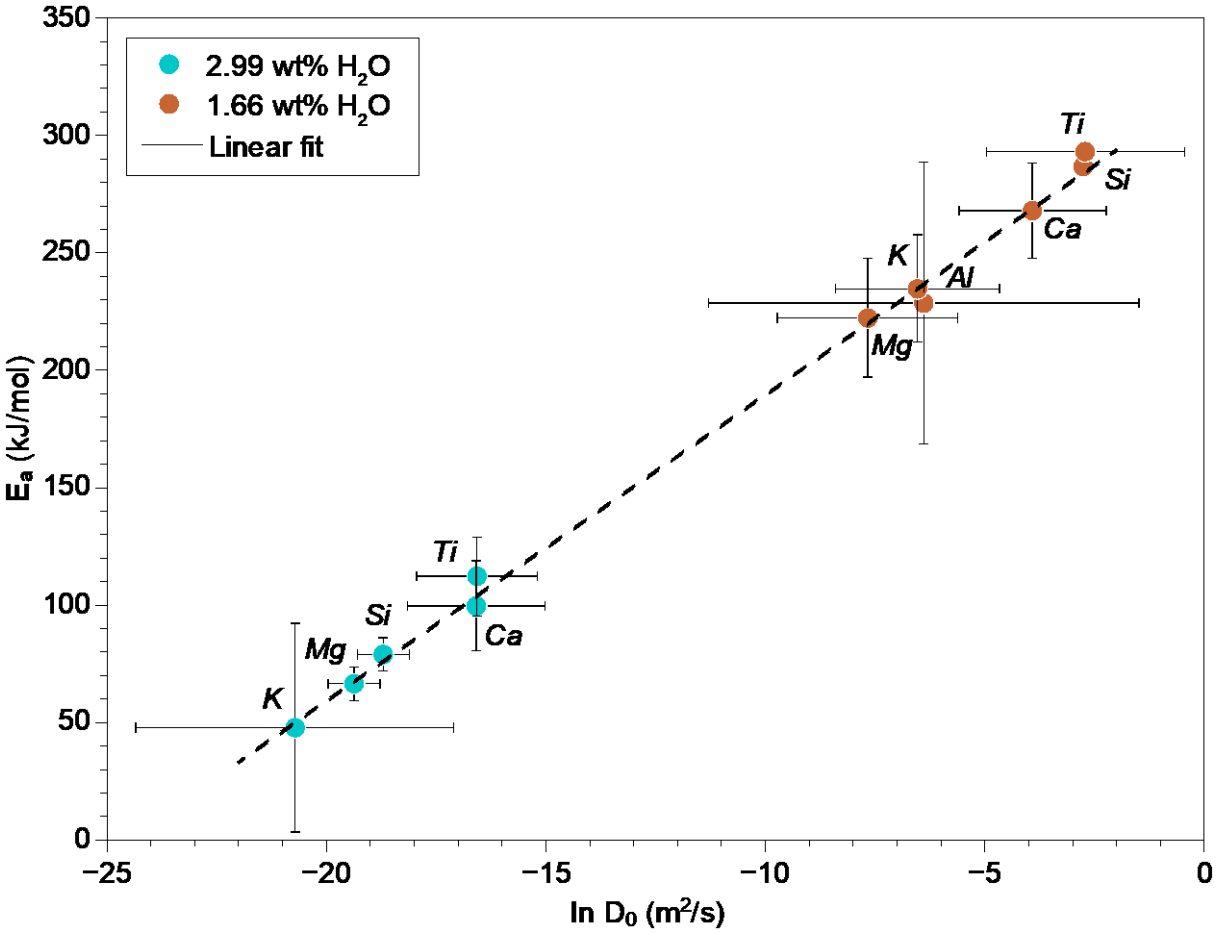

Supplementary figure 4. Plot of Arrhenius parameters lnD_0 vs activation energy (E_a), showing that major elements plot (law of diffusion compensation) along the same linear fit for different H_2O contents.